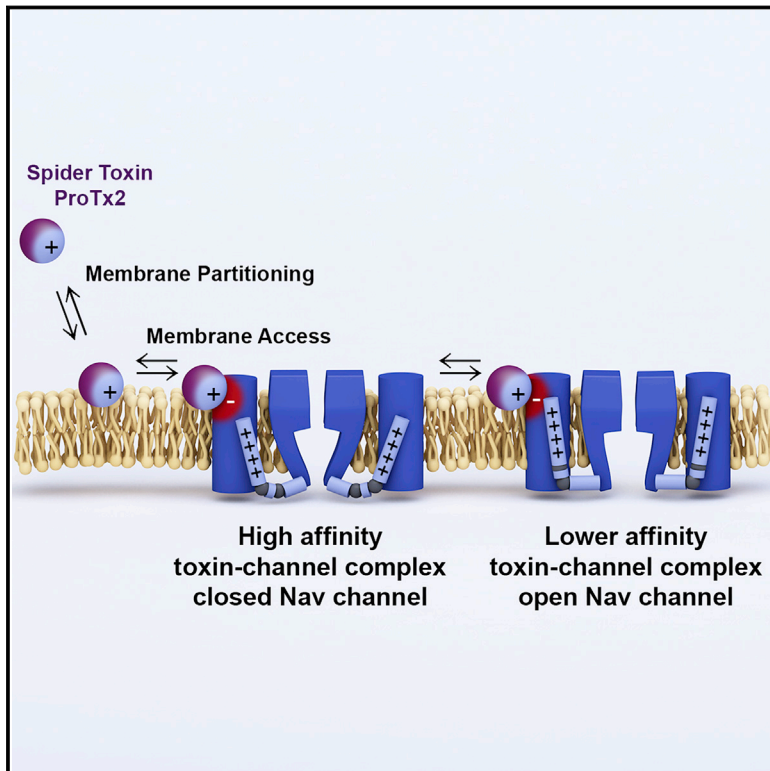


Structural Basis of Nav1.7 Inhibition by a Gating-Modifier Spider Toxin

Graphical Abstract



Authors

Hui Xu, Tianbo Li, Alexis Rohou, ..., David H. Hackos, Christopher M. Koth, Jian Payandeh

Correspondence

li.tianbo@gene.com (T.L.), rohou.alexis@gene.com (A.R.), hackos.david@gene.com (D.H.H.), koth.christopher@gene.com (C.M.K.), payandeh.jian@gene.com (J.P.)

In Brief

Seeing how a spider toxin blocks a sodium channel suggests a structural basis for channel gating and avenues for developing new modulators.

Highlights

- Spider toxin ProTx2 engages the Nav1.7 channel through a membrane access pathway
- The toxin uses an electrostatic mechanism to oppose voltage sensor domain II activation
- The toxin complexes with activated and deactivated states of voltage sensor domain II
- A basis for electromechanical coupling in voltage-gated ion channels is revealed



Structural Basis of Nav1.7 Inhibition by a Gating-Modifier Spider Toxin

Hui Xu,¹ Tianbo Li,^{2,*} Alexis Rohou,^{1,*} Christopher P. Arthur,¹ Foteini Tzakoniati,^{1,5} Evera Wong,³ Alberto Estevez,¹ Christine Kugel,⁴ Yvonne Franke,⁴ Jun Chen,² Claudio Ciferri,¹ David H. Hackos,^{3,*} Christopher M. Koth,^{1,*} and Jian Payandeh^{1,6,*}

¹Department of Structural Biology, Genentech, South San Francisco, CA 94080, USA

²Department of Biochemical and Cellular Pharmacology, Genentech, South San Francisco, CA 94080, USA

³Department of Neuroscience, Genentech, South San Francisco, CA 94080, USA

⁴Department of Biomolecular Resources, Genentech, South San Francisco, CA 94080, USA

⁵Present address: Department of Chemistry, Imperial College London, London, W12 0BZ, UK

⁶Lead Contact

*Correspondence: li.tianbo@gene.com (T.L.), rohou.alexis@gene.com (A.R.), hackos.david@gene.com (D.H.H.), koth.christopher@gene.com (C.M.K.), payandeh.jian@gene.com (J.P.)

<https://doi.org/10.1016/j.cell.2018.12.018>

SUMMARY

Voltage-gated sodium (Nav) channels are targets of disease mutations, toxins, and therapeutic drugs. Despite recent advances, the structural basis of voltage sensing, electromechanical coupling, and toxin modulation remains ill-defined. Protoxin-II (ProTx2) from the Peruvian green velvet tarantula is an inhibitor cystine-knot peptide and selective antagonist of the human Nav1.7 channel. Here, we visualize ProTx2 in complex with voltage-sensor domain II (VSD2) from Nav1.7 using X-ray crystallography and cryoelectron microscopy. Membrane partitioning orients ProTx2 for unfettered access to VSD2, where ProTx2 interrogates distinct features of the Nav1.7 receptor site. ProTx2 positions two basic residues into the extracellular vestibule to antagonize S4 gating-charge movement through an electrostatic mechanism. ProTx2 has trapped activated and deactivated states of VSD2, revealing a remarkable ~ 10 Å translation of the S4 helix, providing a structural framework for activation gating in voltage-gated ion channels. Finally, our results deliver key templates to design selective Nav channel antagonists.

INTRODUCTION

Voltage-gated sodium (Nav) channels initiate action potentials in excitable cells. Mutations in the nine Nav channel subtypes (Nav1.1–Nav1.9) are associated with migraine, epilepsy, pain, and cardiac and muscle paralysis syndromes (Catterall et al., 2005; Huang et al., 2017). Nav channel blockers treat a range of neurological and cardiovascular disorders but lack subtype selectivity due to conservation of the central-pore drug binding site (Payandeh and Hackos, 2018). Genetic studies have identified loss-of-function and gain-of-function mutations in Nav1.7

that result in congenital insensitivity to pain and chronic pain syndromes, respectively (Dib-Hajj et al., 2007). These findings have motivated efforts to develop Nav1.7-selective inhibitors that could overcome the liabilities of non-selective Nav channel blockers and opioid analgesics. However, the discovery of subtype-selective Nav channel drugs remains challenging (McKerrall and Sutherlin, 2018).

Eukaryotic Nav channels contain four voltage-sensor domains (VSD1–4) that surround a central pore module (PM) in a domain-swapped arrangement (Pan et al., 2018). VSDs are helical bundles (S1–S4) that respond to changes in membrane potential by virtue of positively charged arginine residues conserved along the S4 helix in an RxxR motif (Bezaniilla, 2018). Arginine gating charges can move across a narrow hydrophobic constriction within the VSDs into water-accessible vestibules facilitated by interactions with acidic and polar residues from neighboring S1–S3 segments (Groome and Winston, 2013; Pless et al., 2014). Upon membrane depolarization, outward movement of the S4 gating charges appears to couple through intracellular S4–S5 linkers to dilate the S6 helical-bundle crossing to initiate ionic conductance (Muroi et al., 2010). Rapid VSD1–3 activation is required to open the S6 gate (Chanda and Bezaniilla, 2002), whereas VSD4 activation initiates the fast inactivation process (Capes et al., 2013). Because capturing VSDs in a deactivated (i.e., S4-down) state is technically challenging, the structural basis of voltage sensing and electromechanical coupling is still poorly defined. Only coarse models of voltage sensing have been reported (Guo et al., 2016; Kintzer et al., 2018; Li et al., 2014; Takeshita et al., 2014), and structures detailing the electromechanical coupling mechanism between the VSDs and PM have remained elusive.

Peptide toxins that target VSDs have been used to probe the complex gating properties of Nav channels (Gilchrist et al., 2014). These gating modifier toxins include α -scorpion toxins that impede fast inactivation by impairing VSD4 activation (Campos et al., 2008) and β -scorpion toxins that promote channel opening by stabilizing an activated conformation of VSD2 (Cestèle et al., 1998). Toxins that demonstrate Nav channel subtype selectivity have been suggested as potential early drug leads



(Flinspach et al., 2017; Richards et al., 2018), but the ability to optimize toxin potency and selectivity has been hindered due to challenges of producing channels like human Nav1.7 for co-structure determination (Pan et al., 2018).

Protoxin-II (ProTx2) is a 30-residue disulfide-rich peptide isolated from the *Thrixopelma pruriens* tarantula that has unusually high affinity and selectivity toward the human Nav1.7 channel (Flinspach et al., 2017; Middleton et al., 2002; Schmalhofer et al., 2008). ProTx2 is thought to trap VSD2 in a deactivated state, bind only to the S3–S4 loop region, and stabilize the closed channel (Bosmans et al., 2008; Flinspach et al., 2017; Schmalhofer et al., 2008; Smith et al., 2007; Sokolov et al., 2008; Xiao et al., 2010). In contrast to α - and β -scorpion toxins, ProTx2 is a member of the inhibitor cystine knot (ICK) toxin superfamily (Park et al., 2014). ICK toxins are typified by hanatoxin (HaTx1), which can occupy four equivalent VSD binding sites on homotetrameric voltage-gated potassium (Kv) channels (Swartz and MacKinnon, 1997). Intriguingly, HaTx1 potency can be modulated by lipid composition (Milescu et al., 2009), and ProTx2 has been proposed to interact with membrane lipids (Henriques et al., 2016). To better understand how ICK toxins may achieve high potency and selectivity, we set out to define the structural basis for ProTx2 modulation of the human Nav1.7 channel. Because ProTx2 can pharmacologically trap VSD2 in a deactivated state, our results reveal unprecedented insights into voltage sensing and electromechanical coupling and establish new blueprints to design subtype-selective Nav channel antagonists.

RESULTS

ProTx2 Selectively Targets Nav1.7

Using a pulse protocol that favors closed channel states, we verified that ProTx2 shifts the activation of human Nav1.7 to more depolarized potentials (~ 10 mV; $IC_{50} = 0.26$ nM), reduces peak current by $\sim 85\%$, and displays 30- to 100-fold selectivity toward Nav1.7 over other human Nav channel subtypes (Figures 1A and 1B). We next investigated related ICK toxins and found that ProTx2 was among the most potent Nav1.7 antagonists available (Figures S1A–S1C). Notably, GrTx1 diverges only modestly in sequence from ProTx2 but antagonizes Nav1.7 with significantly reduced potency (Figures S1A and S1C).

Production of a ProTx2-VSD2 Complex

To overcome purification challenges for human Nav1.7, we pursued a protein-engineering approach, because VSDs can be transferred onto related channels while retaining their pharmacological properties (Bosmans et al., 2008). In fact, we previously used this approach to visualize VSD4 from Nav1.7 in complex with the small-molecule antagonist GX-936 (Ahuja et al., 2015). We reasoned that the homotetrameric bacterial NavAb channel might facilitate the production of a suitable ProTx2-VSD2 complex (Payandeh et al., 2011).

Replacement of the NavAb VSD with VSD2 from human Nav1.7 enabled purification of a ProTx2-VSD2-NavAb channel complex (Figures S1D–S1F). A small intracellular portion of the NavAb VSD was subsequently reintroduced to facilitate crystallization, as reported for the GX-936-VSD4 structure (Ahuja et al.,

2015) (Figures S1D, S1E, and S1G). We obtained crystals of this optimized ProTx2-VSD2-NavAb complex that diffracted X-rays beyond 3.5 Å resolution (Table S1) when the channel was purified using a facial amphiphile detergent (Lee et al., 2013) and supplemented with phospholipids.

ProTx2-VSD2 Crystallized in a Membrane-like Environment

The ProTx2-VSD2-NavAb channel complex crystallized with a membrane organization, where ProTx2 and the VSD2 receptor site appear unaffected by lattice contacts (Figures 1C, S2A, and S2B). Importantly, no residue from the NavAb channel chassis required for protein expression or crystallization makes contact with ProTx2 (Figures 1C–1E, S2A, and S2B). 16 extra densities were assigned as phospholipids (Figures S2C–S2E), since lipids improved diffraction and acyl-chain detergents were never used during protein or crystal preparation. Overall, the ProTx2-VSD2 complex appears in a membrane-like environment.

We exploited the ICK toxin fold to unequivocally position ProTx2 against the VSD2 receptor site. Pairs of cysteine residues were substituted with selenocysteine (SeCys) and crystals of a derivative complex were subjected to data collection at the selenium absorption edge (Table S1). A strong anomalous difference peak landmarks the C2–C16 disulfide bond of ProTx2 within the crystal lattice (Figure 1D). We similarly collected and analyzed data from a selenomethionine (SeMet) ProTx2-derivative complex (Figure 1D and Table S1). Simple geometric considerations using an available atomic structure of ProTx2 (Wright et al., 2017) lead to unambiguous placement of the toxin against VSD2, consistent with unbiased density observed in our 3.5 Å resolution native dataset (Figure S3A and Table S1).

The global topology of the ProTx2-VSD2-NavAb channel complex is in agreement with the ability to modify the amino-terminus of ProTx2 (Figures S1F–S1H). To further corroborate residue assignments, we analyzed anomalous difference peaks from a SeMet-VSD2-NavAb channel derivative complex (Figures S2F and S2G and Table S1). Finally, we performed cryoelectron microscopy (cryo-EM) analysis (Figures S4A–S4D) and obtained nominal resolutions of ~ 5 Å around the VSD2 receptor site (Figures S5A–S5E), which independently validated the structural model derived from crystallographic analysis. Below, we first focus on the higher-resolution crystal structure of the ProTx2-VSD2-NavAb channel complex.

Overall Structure of the ProTx2-VSD2 Complex

The ProTx2-VSD2-NavAb channel complex is reminiscent of a four-point ninja throwing star, where the tips of the star are occupied by toxin (Figure 1C). ProTx2 attacks VSD2 from the extracellular membrane leaflet (Figures 1C–1E), where the toxin partitions using an amphipathic surface patch that buries ~ 350 Å² within the membrane. ProTx2 is constrained only by the membrane-aqueous interface and a few residues contributed from VSD2 (Figures 1C–1E and S3A). The structure provides the impression that membrane partitioning positions ProTx2 for unobstructed access to the peripheral VSD2 receptor site.

Immersion of ProTx2 at the membrane-aqueous interface is compatible with biophysical studies on ICK toxins and partial

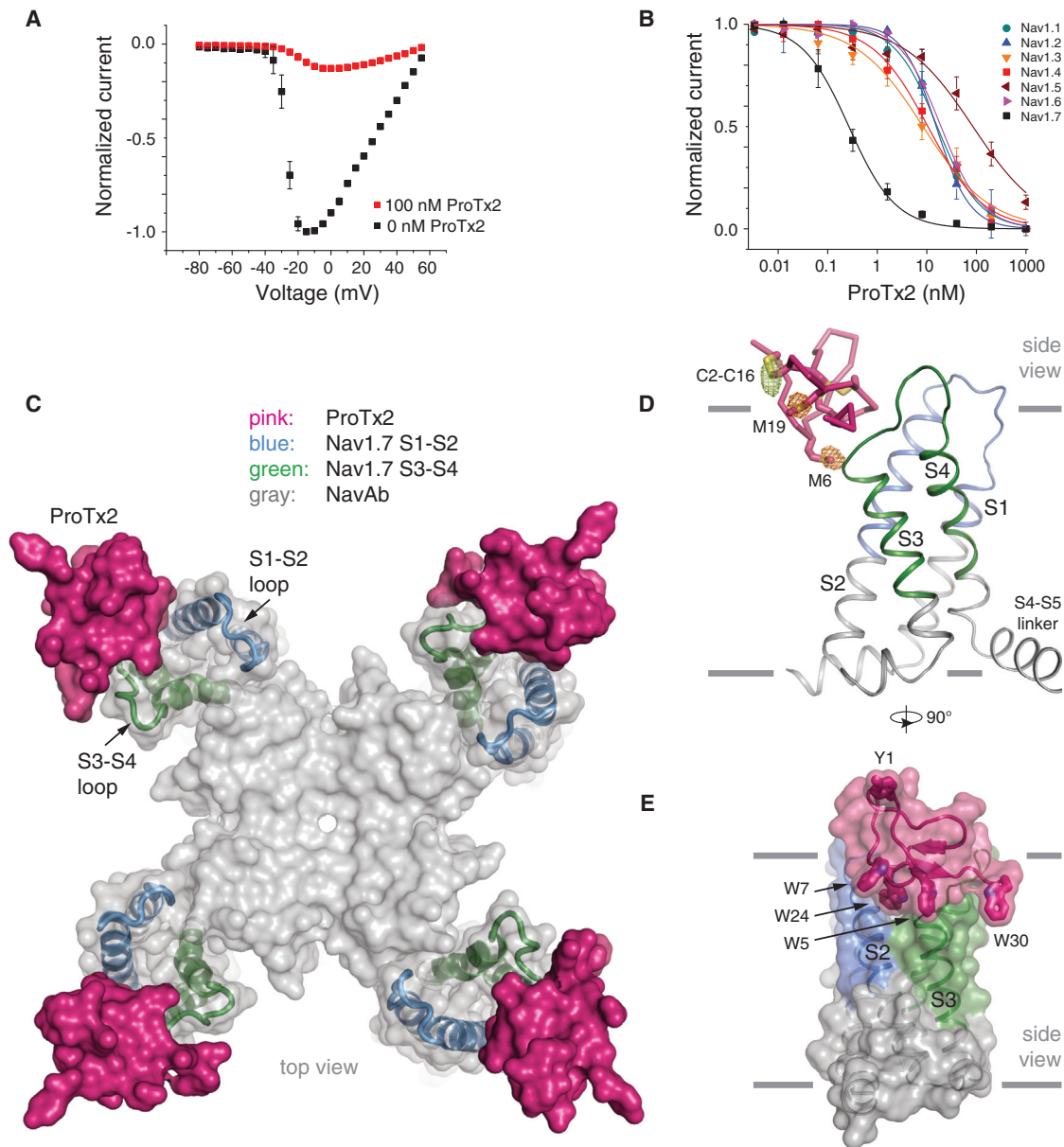


Figure 1. Crystal Structure of the ProTx2-VSD2-NavAb Channel Complex

(A) Human Nav1.7 peak currents \pm 100 nM ProTx2. Error bars represent mean \pm SEM.

(B) Potency of ProTx2 on human Nav channels. Error bars represent mean \pm SEM.

(C) ProTx2-VSD2-NavAb channel crystal structure, top view, with human Nav1.7 VSD2 portion shown in blue (S1–S2) and green (S3–S4).

(D) Membrane view highlighting anomalous difference peaks from SeCys2–SeCys16 (yellow mesh, 4 σ) and SeMet-ProTx2 derivatives (orange mesh, 3.25 and 2.75 σ , M6 and M19, respectively).

(E) Membrane view highlighting Y1, W5, W7, W24, and W30 on ProTx2.

See also [Figures S1, S2, S3, and S6](#) and [Table S1](#).

lipids modeled alongside ProTx2 ([Figures S2C–S2E](#)) ([Henriques et al., 2016](#); [Lee and MacKinnon, 2004](#); [Mihailescu et al., 2014](#); [Milescu et al., 2009](#)). An aromatic-rich surface including W5, W7, W24, and W30 anchors ProTx2 \sim 5 Å toward the membrane core relative to lipid headgroups bound along the PM ([Figures 1D, 1E, and S2D](#)). ProTx2 contains a polybasic C-ter-

минаl tail (K26–K27–K28) capped by a hydrophobic dyad (L29–W30) that further anchors the toxin into the membrane while positioning it over the S3 helix ([Figures 1E and S3A](#)). Membrane interdigitation and juxtaposition of the C-terminal tail against VSD2 rationalizes why toxin modifications in this region can appreciably impact potency and selectivity toward

Nav channels (Flinspach et al., 2017; Park et al., 2014; Smith et al., 2007).

Features observed for ProTx2 define the VSD2-bound form as a peripheral membrane protein. Membrane partitioning of the amphipathic toxin should concentrate ProTx2 toward Nav1.7, decrease its rotational freedom, and enforce a two-dimensional receptor-site search (Henriques et al., 2016; Lee and MacKinnon, 2004; Mihailescu et al., 2014). These pharmacological features undoubtedly combine to impart high affinity and selective binding of ProTx2 to Nav1.7.

ProTx2 in Complex with an Activated VSD2

The ProTx2-VSD2 crystal structure illuminates molecular details of toxin binding, selectivity, and antagonism of Nav channels. With unobstructed access from the bulk membrane, ProTx2 is perched directly on top of the S3 helix of VSD2, the most peripherally exposed structural element in Nav channels (Figures 1C and 1D). VSD2 adopts an activated conformation (Figures 2A–2C), consistent with the biochemical conditions of our samples. Accordingly, the R4 gating charge forms characteristic ion-pairing interactions with the intracellular negative-charge cluster (INC), thereby positioning the R1–R3 gating charges above the hydrophobic constriction site (HCS; Figures 2A and 2B). The R2 and R3 gating charges form interactions with conserved acidic and polar residues of the extracellular negative-charge cluster (ENC; Figures 2A and 2B). The S4 transitions from an α helix into a 3_{10} -helix across the HCS and then evolves through an α -helical conformation into the S3–S4 loop (Figures 2D and 2E). The S3–S4 loop is not fully resolved in electron density, highlighting its potential mobility (Figures S3B and S3C).

ProTx2 shifts the activation of Nav1.7 to more positive potentials (Figure 1A), so it may seem surprising to find VSD2 in an activated state (Figures 2A and 2B). However, HaTx1 has been shown to bind to both activated and deactivated states of the VSDs in Kv channels and can remain bound even when VSDs transition between states (Phillips et al., 2005; Swartz and MacKinnon, 1997). Capturing ProTx2 in complex with an activated VSD2 aligns with these findings. In fact, ProTx2 antagonizes Nav1.7 with only ~ 60 -fold lower potency when the membrane potential is held at a voltage that promotes the activated state of VSD2 (IC₅₀ at 0 mV ~ 15 nM; Figures 2F). The small binding footprint that ProTx2 has on VSD2 (~ 750 Å²), along with the apparent S3–S4 loop mobility (Figures S3B and S3C), can rationalize why S4 gating charges might still translocate across the HCS in toxin-modified Nav1.7 channels.

Superposition of the ProTx2-VSD2 complex onto available VSD structures corroborates the assignment of an activated state (Figures 2C) (Guo et al., 2016; Li et al., 2014; Long et al., 2007; Pan et al., 2018; Takeshita et al., 2014). Comparison to the GX-936-VSD4 complex is particularly informative because GX-936 is a potent small molecule antagonist known to stabilize VSD4 in an activated state (Figures 2C) (Ahuja et al., 2015). VSD2 and VSD4 share similar core structures in their respective activated states (Figures 2C and 2D). While a FLAD (Phe-Leu-Ala-Asp) motif is found in both VSD2 and VSD4, the S3 helix in VSD4 extends two helical turns beyond the VSD2 S3 helix (Figures 2D, 2E, and S6A). Since ProTx2 docks on top of the VSD2 S3 helix from the membrane, the toxin is precluded from

approaching VSD4 in a similar binding mode without significant clashes or rearrangements of VSD4 (Figures 2D and 2E).

Determinants of ProTx2 Binding to VSD2

Elucidation of the ProTx2 receptor site reveals the molecular determinants of selective Nav1.7 channel targeting. Scanning mutagenesis across VSD2 confirms that the LFLAD motif in the S3–S4 loop region (L812-F813-L814-A815-D816) is the major receptor site hotspot (Figures 3A–3C) (Schmalhofer et al., 2008). As ProTx2 approaches VSD2 from the extracellular membrane leaflet, the receptor site can be divided into two zones: a membrane-partitioned interface and a polar interface (Figure 3B).

At the membrane-partitioned interface, ProTx2 wedges its bulky W24 side-chain into a cleft formed between the lipid-facing S2 and S3 helices (Figures 3B and 3C). W24 is one of few ProTx2 residues that makes intimate contacts with the receptor site (Figures 3B–3E and S3A), and it docks into a hydrophobic shelf formed by A766 (S2), L770 (S2), and L812 (S3) (Figure 3C). The indole nitrogen of W24 bonds to the backbone carbonyl of L812 to cap the extracellular end of the S3 helix (Figures 3C and 3D). L770 and L812 are highly conserved across human Nav channels (Figure S6B), and mutagenesis indicates that the L812 side chain is critical for stabilizing the hydrophobic shelf (Figures 3A and 3C). A766 makes limited contacts with ProTx2 (L23 and W24), explaining why mutation to leucine (A766L) does not alter toxin potency (Figure 3A), but this position is a polar side chain in most Nav channel subtypes (Figure S6B). Overall, W24 functions as a hydrophobic anchor and key attachment point that stabilizes ProTx2 for productive receptor site engagement.

W5 and M6 from ProTx2 align along the membrane-partitioned interface to flank F813, an established Nav1.7 selectivity determinant of ProTx2 (Schmalhofer et al., 2008; Xiao et al., 2010) (Figure 3C). W5 and M6 form slight hydrophobic and van der Waals interactions with F813 (Figure 3C), and a ~ 4 -fold reduction in potency is measured when F813 is truncated to alanine (Figure 3A). The F813C substitution, which introduces a more polar side chain, similarly reduces ProTx2 potency (Figures 3F and 3G) (Xiao et al., 2010). A serine should likewise perturb the receptor site (Schmalhofer et al., 2008), consistent with the lower potency of ProTx2 toward Nav1.6 (Figures 1A and S6B). Glycine is substituted at position F813 in other Nav channel subtypes (Figure S6B), and glycine has the lowest helical propensity among all α -amino acids. Thus, glycine-mediated destabilization of the S3 helix may reduce ProTx2 binding to these Nav channel subtypes (Schmalhofer et al., 2008; Xiao et al., 2010), perhaps by perturbing the L812 carbonyl for productive interaction with W24 (Figures 3C–3E). We conclude that the high-affinity ProTx2 receptor site on Nav1.7 VSD2 provides a stable S3 helix onto which the toxin can readily dock from the bulk membrane phase.

ProTx2 does not directly engage the S1–S2 region of VSD2 beyond limited hydrophobic contacts to A766 and L770 on the S2 helix (Figures 3B and 3C). However, the I767A mutation appreciably reduces ProTx2 potency (Figure 3A). I767 (S2) is membrane facing and abuts an electron density assigned as a partial phospholipid (Figures S2C–S2E). The headgroup of this lipid is within hydrogen-bonding distance to T8 on ProTx2, suggesting that I767 may help to orchestrate a tripartite

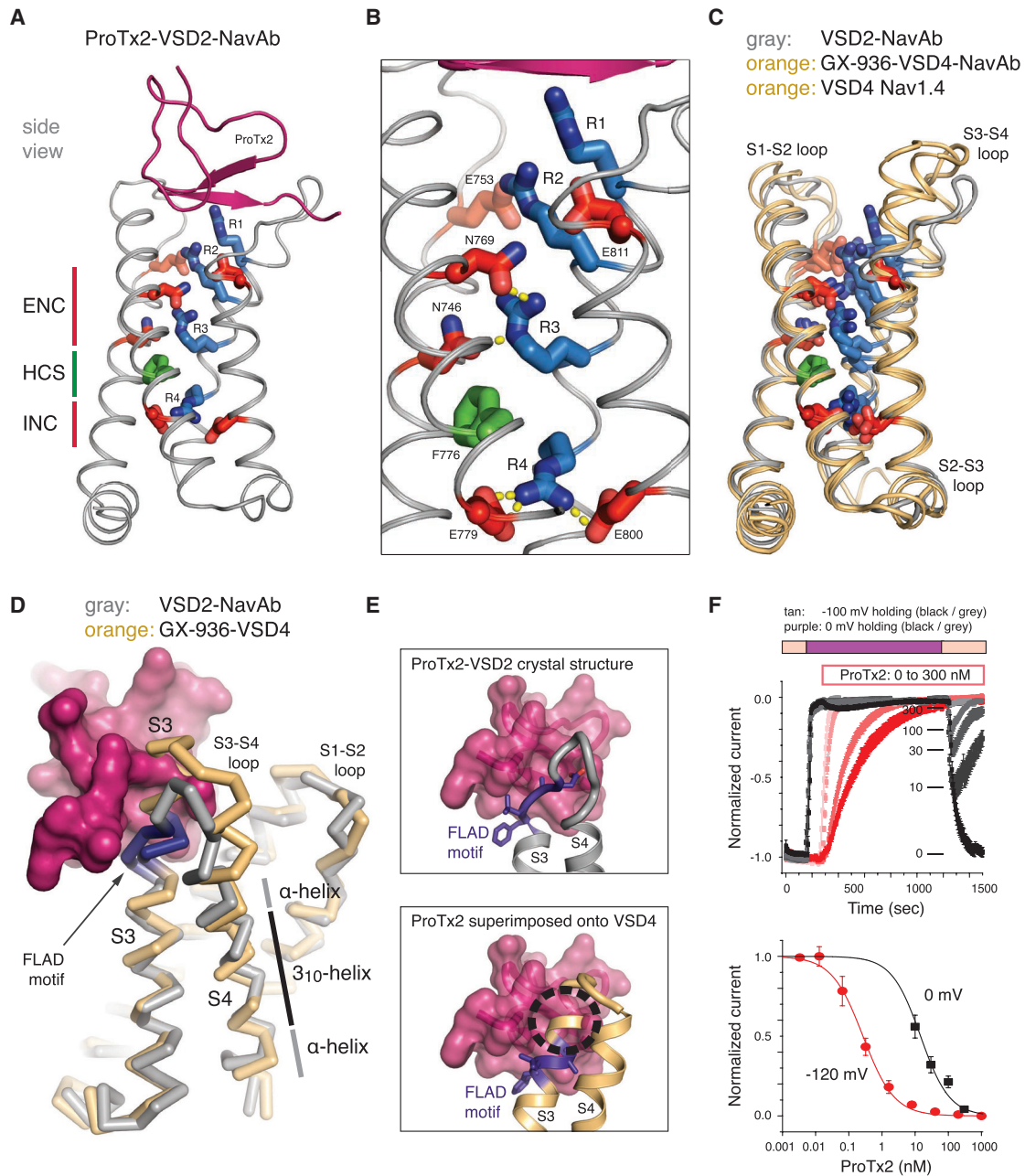


Figure 2. ProTx2-VSD2-Activated State Complex

(A) View highlighting ENC, HCS, and INC side chains; S4 gating charges are in blue.

(B) View of activated VSD2.

(C) VSD2 (ProTx2 omitted) with VSD4 from Nav1.4 (PDB: 6AGF) and Nav1.7 (PDB: 5EK0, GX-936 omitted) superimposed.

(D) Alternate view of (C), with ProTx2 shown (pink surface).

(E) Close-in view of (D) including an incompatible ProTx2-VSD4 model based on VSD2 superposition.

(F) Upper panel: Nav1.7 peak currents elicited from holding voltage (V_m) at -100 mV (red) or switching between -100 to 0 mV (black/grey) with 0 – 300 nM ProTx2. The recovered current after switching V_m back to -100 mV from 0 mV was used to measure the level of unblocked current at 0 mV. Comparison with closed-state controls (red; V_m at -100 mV throughout) indicates that holding at 0 mV decreases ProTx2 potency. Lower panel: ProTx2 potency on Nav1.7 at a holding potential of -120 mV (red) or 0 mV (black), respectively. Error bars represent mean \pm SEM.

See also [Figures S3](#) or [S6](#).

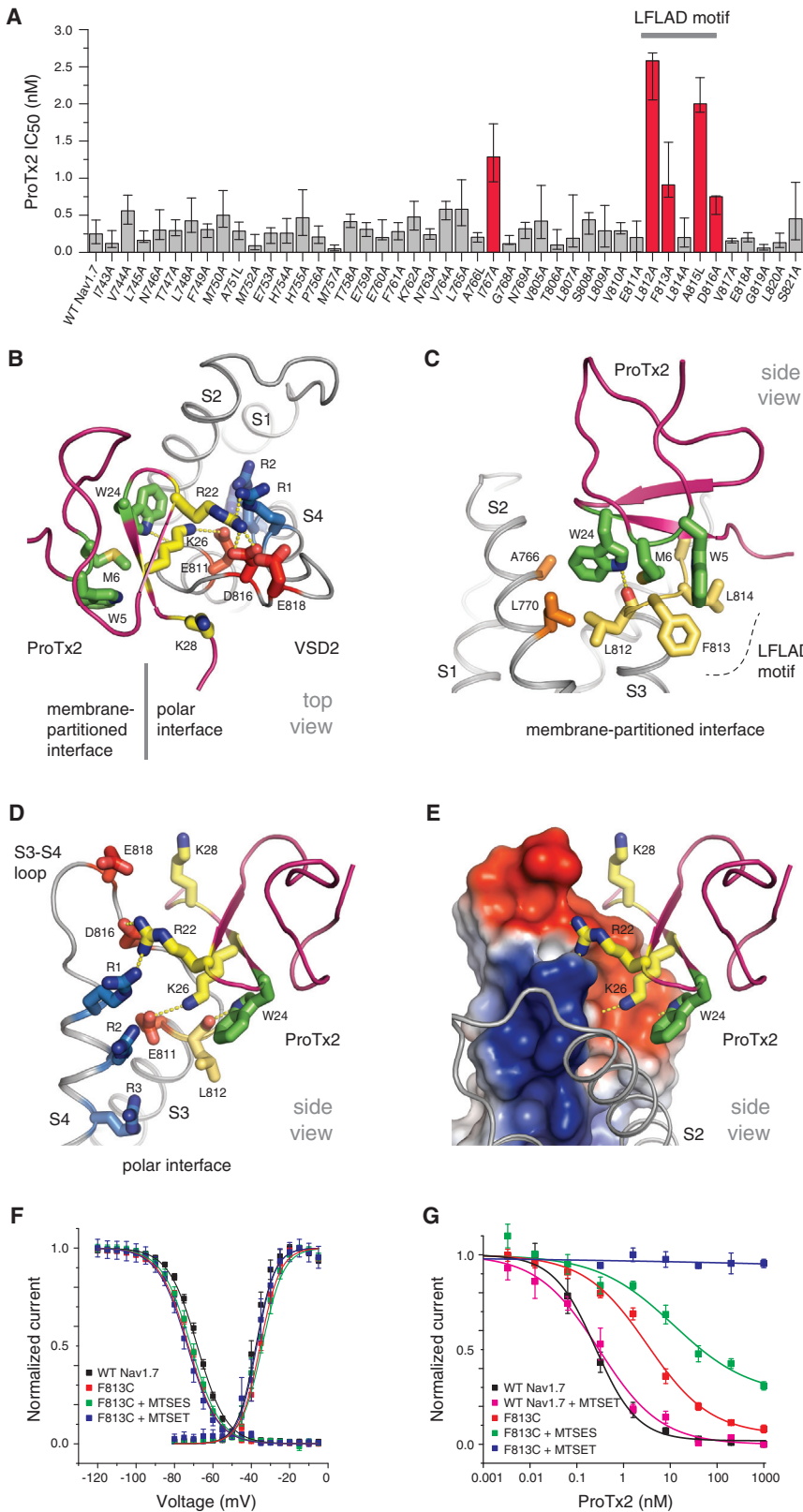


Figure 3. VSD2 Receptor Site for ProTx2

(A) Potency of ProTx2 on human Nav1.7 mutants (by 95% confidence interval IC₅₀) using a pulse protocol that favors closed channel states.

(B) ProTx2-VSD2 interface, extracellular view. Hydrogen bond and ionic interactions are indicated by yellow dotted lines.

(C) Membrane perspective of the ProTx2-VSD2 interface. Hydrogen bond (3.2 Å) between W24 and L812 is indicated.

(D) S3-S4 region of the polar interface. Interactions between R22 with D816 (2.6 Å) and R1 (2.8 Å), as well as K26 with E811 (~3.5 Å), are highlighted.

(E) As in (D), with the S3-S4 region shown as electrostatic surface.

(F) Characteristics of wild-type (WT) and F813C channels ± MTS reagents. Error bars represent mean ± SEM.

(G) Potency of ProTx2 measured ± MTS modifying reagents. MTSET is positively charged. Error bars represent mean ± SEM.

See also Figures S3 and S6.

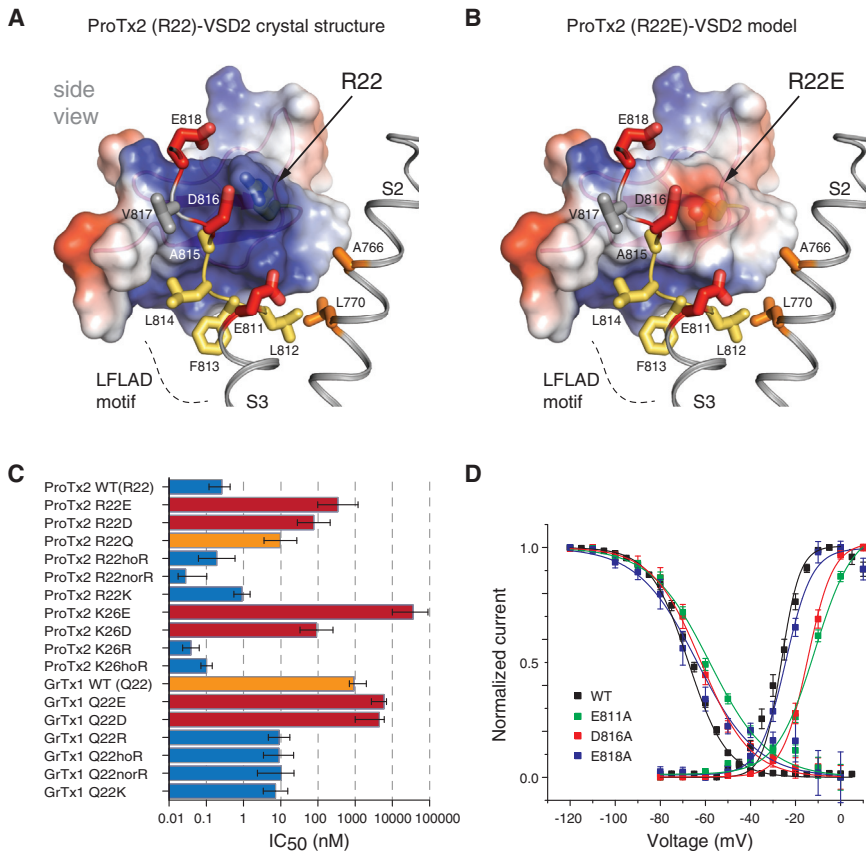


Figure 4. ProTx2 Positions 22 and 26 Modulate the Nav1.7 Channel

(A) Pore view of the ProTx2 receptor site. Electrostatic surface of ProTx2 with R22 highlighted. (B) Similar to (A); ProTx2-R22E variant modeled. (C) Potency of ProTx2 and GrTx1 derivatives measured on human Nav1.7 (by 95% confidence interval IC₅₀) using a pulse protocol that favors closed channel states.

(D) Characteristics of WT and E811A, D816A, and E818A channels. Error bars represent mean \pm SEM.

See also Figure S6 and Table S3.

underlie the molecular logic that determines the potency and selectivity of ProTx2, precluding definition of a single interaction network between the toxin and VSD2.

ProTx2 acts as an Electrostatic Gating Modifier

The ProTx2-VSD2 structure clarifies the mechanism of Nav channel modulation by ICK toxins. Remarkably, ProTx2 extends two basic side chains into the extracellular vestibule of VSD2 (Figures 3D, 3E, and 4A). The structure invokes a simple mechanism to antagonize Nav1.7: by inserting positive charges into VSD2, ProTx2 acts as an electrostatic modulator to alter gating-charge

movement. From their opportune location, R22 and K26 are positioned to antagonize outward gating-charge movement through direct electrostatic repulsion (Figures 3D, 3E, and 4A). Alternatively, R22 and K26 may indirectly antagonize S4 gating-charge movement by neutralizing acidic side chains within the extracellular vestibule of VSD2 (Figures 3D, 3E, 4A, and 4B).

ProTx2-lipid-VSD2 complex (Figure S2E). This speculation emphasizes the membrane-access mechanism of ProTx2 and is reminiscent of other tetrameric channel-modulator complexes (Ahuja et al., 2015; Gao et al., 2016; Milesescu et al., 2009). The polar interface of the VSD2 receptor site contributes to ProTx2 potency and selectivity since residues within the S3–S4 loop are not conserved across all Nav channels (Figure S6B). Three tiers of acidic side chains dominate this interface to impart an imposing electronegative character: E811 on the S3 helix, D816 in the LFLAD motif hotspot, and E818 at the apex of the S3–S4 loop (Figures 3D and 3E). This constellation of residues likely serves as part of the ENC in VSD2. Homology modeling indicates that S3–S4 loop electrostatics may rationalize subtype selectivity of ProTx2 beyond the side-chain composition at positions A766 (S2) and F813 (S3) (Figures S6B–S6D). Conversion of the VSD2-LGLAN motif in Nav1.2 into an LFLAD motif increases ProTx2 potency by >20-fold (Figure S6E), confirming that a helix-stabilizing residue (F813) and an acidic side chain (D816) are key drivers of ProTx2 selectivity toward Nav1.7. Most notably, ProTx2 extends two basic side chains into the extracellular vestibule of VSD2 (Figures 3B, 3D, and 3E). R22 of ProTx2 crosses over E811 (S3) and under E818 (S3–S4 loop) to engage D816 (LFLAD motif) as it reaches the R1 gating charge on the activated S4 helix, while K26 directly engages E811 on the S3 helix through a salt-bridge interaction (Figures 3D and 3E). As we demonstrate below, multivalent and adjustable polar-interface interactions

movement. From their opportune location, R22 and K26 are positioned to antagonize outward gating-charge movement through direct electrostatic repulsion (Figures 3D, 3E, and 4A). Alternatively, R22 and K26 may indirectly antagonize S4 gating-charge movement by neutralizing acidic side chains within the extracellular vestibule of VSD2 (Figures 3D, 3E, 4A, and 4B).

To evaluate the hypothesis that ProTx2 functions as an electrostatic gating modifier, we first probed geometric parameters required for Nav1.7 modulation. Substituting R22 with homo-arginine (hoR) or nor-arginine (norR), which extend or shorten the side chain by one methylene unit, produces toxin derivatives with similar potencies as wild-type ProTx2 (Figure 4C). These results are consistent with the structure and the molecular promiscuity afforded by a guanidino side chain. ProTx2-R22norR displayed a \sim 10-fold potency increase toward Nav1.7 (Figure 4C), hinting at subtle interaction differences within the receptor site. A lysine derivative demonstrated that a guanidino group at position 22 is not formally required for potent modulation of Nav1.7 by ProTx2 (Figure 4C).

Disparate chemistries at position 22 in ProTx2 were next investigated by substitution of R22 to glutamate or aspartate. From structural modeling, the long acidic side chain of glutamate may appear to interact favorably with the R1 and R2 gating charges (Figure 4B); however, the toxin derivatives ProTx2-R22E and ProTx2-R22D showed \sim 300-fold lower potency

toward Nav1.7 (Figure 4C). These results indicate that the position 22 side-chain is most likely to encounter the electronegative potential contributed by E811, D816, and E818 within the receptor site (Figures 3D, 3E, 4A and 4B). Consistent with this interpretation, the toxin derivative ProTx2-R22Q showed an intermediate potency between variants harboring a basic or acidic side chain at position 22 (Figure 4C).

To evaluate if simply placing a charge proximal to the extracellular vestibule of VSD2 is sufficient to modulate Nav1.7, we exploited our F813C channel (Figure 3F). Chemical modification of F813C by the positively charged 2-(trimethylammonium)ethyl methanethiosulfonate (MTSET) reagent or the negatively charged 2-sulfonatoethyl methanethiosulfonate (MTSES) reagent had no effect on channel gating (Figure 3F). However, F813C-MTSET-modified channels became resistant to ProTx2 modulation (Figure 3G), likely due to repulsion of the basic surface patch on ProTx2 (Figure 4A). These findings confirm that the architecture of the ProTx2-VSD2 complex is required to impact gating and suggest that VSD2 is the only relevant receptor site on the Nav1.7 channel.

To further probe if ProTx2 functions as an electrostatic gating modifier, basic and acidic derivatives of K26 were examined and followed similar trends as the position 22 toxin variants (Figure 4C). In fact, the ProTx2-K26hoR and ProTx2-K26R derivatives showed 2- to 10-fold increased potency (Figure 4C). In the ProTx2-VSD2 structure, K26 directly neutralizes E811 (Figures 3D and 3E), a conserved acidic residue on the S3 helix that may impact gating in other Nav channels (Huang et al., 2017). Remarkably, the E811A mutation by itself had a significant impact on Nav1.7 channel activation, shifting the V_{50} toward 0 mV (Figure 4D) as if to mimic ProTx2 modulation. Evaluation of other Nav1.7 channel constructs showed that the D816A mutation also imparts a rightward shift on the V_{50} toward 0 mV (Figure 4D), very reminiscent of ProTx2 modulation. These biophysical results establish that E811 and D816 are functional ENC residues in VSD2 of Nav1.7 and confirm that ProTx2 imparts channel modulation by directly targeting them. In fact, the side-chain character at positions 22 and 26 of ProTx2 appears to set a threshold for the potency of Nav1.7 modulation (Figure 4C).

Position 22 is a Gating Modifier Hotspot in ICK Toxins

Compelled by our ProTx2 derivative results, we leveraged a related ICK toxin to further evaluate the electrostatic gating modifier hypothesis. GrTx1 naturally harbors a glutamine at position 22 and shows only modest potency against human Nav1.7 (Figures S1A and S1C) (Redaelli et al., 2010). However, all GrTx1 derivatives with a positive charge (R, hoR, norR, and K) substituted into position 22 displayed ~ 100 -fold improved potencies toward Nav1.7 (Figure 4C), indicating that these variants likely form inhibitory complexes analogous to ProTx2-VSD2. Conversely, acidic substituted derivatives GrTx1-Q22D and GrTx1-Q22E maintained low potency toward Nav1.7 (Figure 4C). These data support the premise that ProTx2 antagonizes S4 gating-charge movement by neutralizing acidic residues within the extracellular vestibule of VSD2.

If ProTx2 and GrTx1 modulate Nav1.7 through an electrostatic mechanism, toxin variants should also modify voltage-depen-

dent channel gating. Position 22 substitutions do alter the voltage-dependent properties of Nav1.7 (Table S3), but the complex outcomes observed likely reflect the multifaceted interaction networks seen in the ProTx2-VSD2 structure (Figures 3B–3E and 4A). Consistent with an electrostatic mechanism, the potencies of ProTx2, position 22 derivatives, and GrTx1 are also reduced with increasing ionic strength relative to the pore-blocker tetrodotoxin (Figure S6F). We conclude that position 22 in ProTx2 and GrTx1 functions as an electrostatic gating modifier capable of fine-tuning toxin potency and Nav channel activation.

Cryo-EM Captures Two States of the ProTx2 Receptor Site

To gain further insights into ProTx2 modulation of Nav1.7, we performed cryo-EM analysis of a ProTx2-VSD2-NavAb-Fab complex (Figures S4A–S4D and S5A–S5E and Table S2) under detergent and lipid conditions matched to our crystallization sample. Two distinct channel conformations were identifiable from our three-dimensional reconstructions, which we refer to as ProTx2-VSD2-activated and ProTx2-VSD2-deactivated states, respectively (Figures 5A–5F, 6A–6F, S4D, and S5A–S5E and Video S1). Resolutions range from ~ 3.5 Å in the channel PM to ~ 5 Å at the VSD2 receptor site (Figures S5A and S5C), allowing ProTx2 to be placed as a rigid body and most S4 helix side chains to be resolved (Figures 5A, 5B, and S5E). Visualization of discrete VSD activation states is uncommon (Kintzer et al., 2018; Li et al., 2014), so these results provide templates to explore the structural basis of voltage sensing and electromechanical coupling in canonical voltage-gated ion channels.

The ProTx2-VSD2-activated state structure resembles our crystallographic model (Figures 5A, 5C, 5E, S5D, and S5E) with a modest ~ 2 Å translation of the S1–S2 helices within the membrane plane. In the absence of a crystal lattice, a slight repositioning of ProTx2 and minor movements of the S3–S4 loop are observed (Figures 5A and 5C). K26 and W24 from ProTx2 target S3 helix residues E811 and L812, respectively, and R22 appears to engage D816 from the S3–S4 loop (Figure 5E). Overall, this cryo-EM structure further supports our prior mechanistic interpretations.

Cryo-EM analysis revealed 18.5% of classified particles to have VSD2 in a deactivated state (Figures 5B–5D, 5F, S5D, and S5E). Despite our use of a chimeric protein construct and solution conditions, this striking result likely reflects the ability of ProTx2 to right shift the activation of Nav1.7 and pharmacologically stabilize a closed channel state (Figure 1A). Consistent with the protocol used in our scanning mutagenesis study (Figure 3A), the receptor site targeted by ProTx2 does not extend to additional regions relative to the ProTx2-VSD2-activated state structure. In fact, the extracellular S2–S3 interface undergoes limited rearrangement, indicating that W24 likely anchors ProTx2 against VSD2 in both states (Figures 5C, 5E, and 5F). However, the remainder of the receptor site has undergone considerable rearrangements in the VSD2-deactivated state.

ProTx2 traps VSD2 in a deactivated state where the S4 helix has translated ~ 10 Å downward (Figure 5C), and consequently, the S3–S4 loop has shifted by ~ 7 Å to reposition E818 atop the S4 helix. Therefore, the deactivated state presents the S3-helical

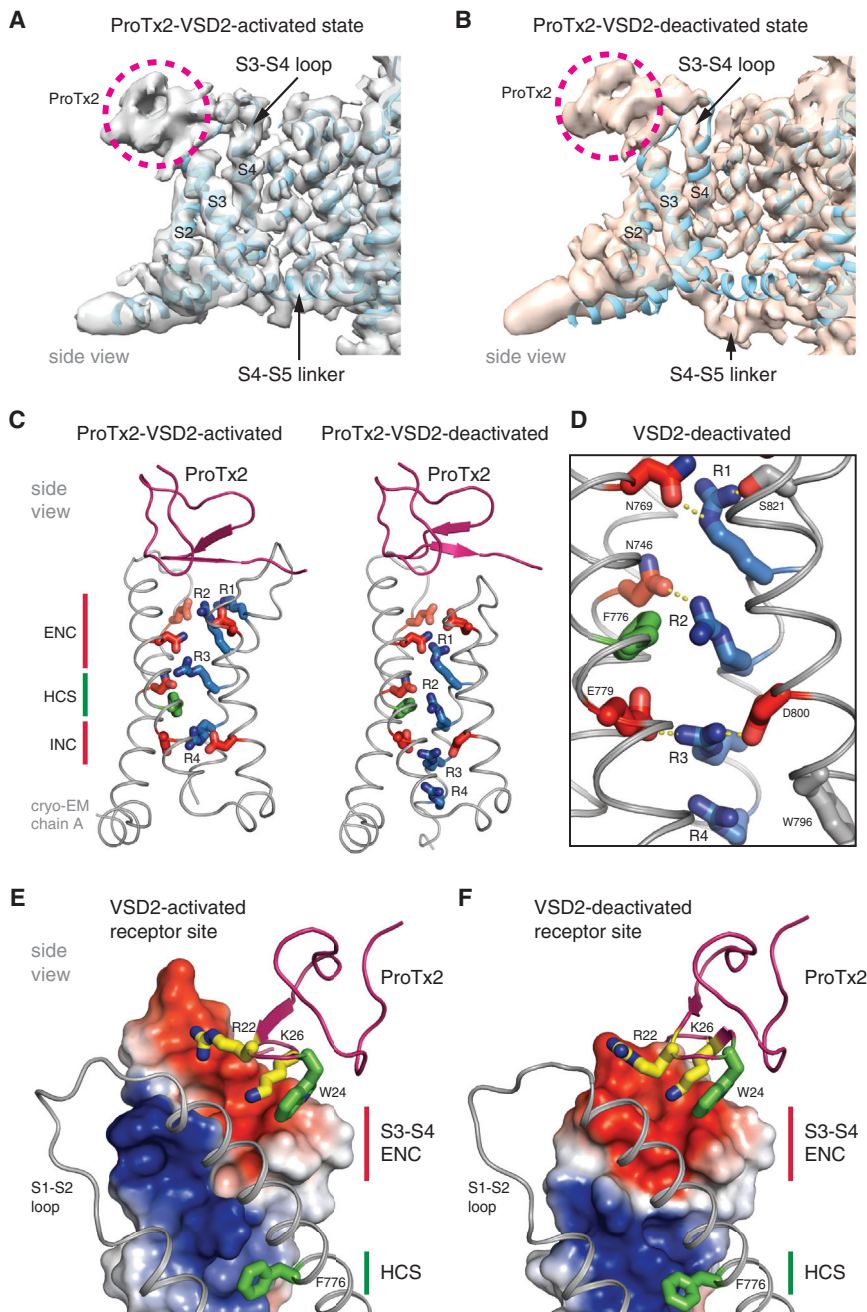


Figure 5. Cryo-EM Structures of ProTx2 Bound to Activated and Deactivated States of VSD2

(A) Surface of a cryo-EM map of ProTx2-VSD2 activated state (gray) with the ProTx2-VSD2-NavAb crystal structure (cyan) imposed for comparison.

(B) Cryo-EM map of ProTx2-VSD2 deactivated state (orange) with the ProTx2-VSD2-NavAb crystal structure imposed for comparison.

(C) VSD2 in activated and deactivated states; chain A is shown. R1 in the cryo-EM structure of the VSD2-activated state is poorly resolved.

(D) View of deactivated VSD2.

(E) S3-S4 region of the cryo-EM VSD2 activated state shown as an electrostatic surface with S1-S2 region shown for reference.

(F) VSD2-deactivated state, similar to (E). Note R22 side chain is poorly resolved.

See also [Figures S4 and S5](#); [Table S2](#); and [Videos S1, S2, and S3](#).

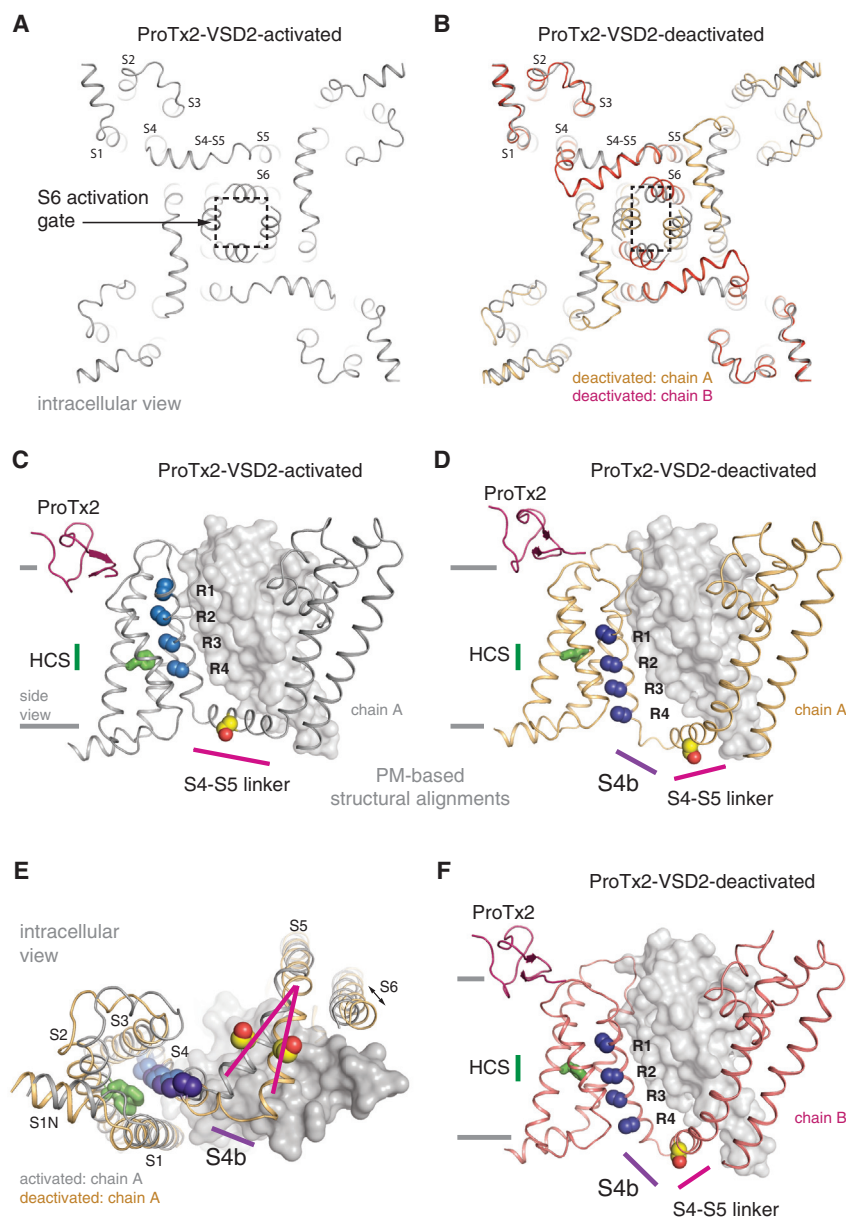
and highlight the electrostatic mechanism of Nav channel modulation by ProTx2. Thus, our cryo-EM analysis has revealed a dynamic VSD2 receptor site and the capacity of ProTx2 to achieve high affinity and selectivity for Nav1.7 using only a small interaction surface.

Activation and Gating-Charge Transfer in VSD2

The structural basis of voltage sensing in VSD2 has remained elusive but can now be appreciated by comparing ProTx2-VSD2-activated and ProTx2-VSD2-deactivated state structures. The ProTx2-VSD2-activated conformation is typical of most VSDs visualized at 0 mV potential and recapitulates the core scaffold of VSD4 from Nav1.4 and Nav1.7 ([Figure 2C](#)) ([Ahuja et al., 2015](#); [Pan et al., 2018](#)). In the VSD2-activated state, the R4 gating charge is housed beneath a conserved S2 phenylalanine side-chain (F776) within the intracellular vestibule ([Figure 5C](#)), a location known as the charge-transfer center (CTC) in Kv channels ([Tao et al., 2010](#)).

F776 forms part of a narrow HCS thought to focus the membrane electric field across the VSD. Physiological measurements indicate that when the R4 gating-charge equivalent is housed within the CTC, the VSD is in an activated conformation ([Bezanilla, 2018](#); [Tao et al., 2010](#)). Therefore, the ProTx2-VSD2-deactivated state structure unequivocally reveals a distinct conformation because only the R1 gating charge remains strictly above the HCS within the extracellular vestibule ([Figures 5C and 5D](#)).

Cataloguing gating charge locations in VSD2 provides insight into VSD activation, where changes in S4 conformation are



appreciated by measurements between equivalent C_{α} -backbone atoms: R1-R1 (~ 11 Å), R2-R2 (~ 12 Å), R3-R3 (~ 11.5 Å), and R4-R4 (~ 11 Å) (Figures 5C and 6C–6F and Video S2). In the VSD2-deactivated state, the S4 exists primarily in a 3_{10} -helical conformation, which serves to align gating charges across the HCS (Figure 5D). Specifically, R1 coordinates to N769 (ENC, S2) and S821 (S4) above the HCS, R2 interacts with both N746 (ENC, S1) and the HCS, R3 is engaged with INC residues below the canonical CTC site, and R4 aligns along a conserved tryptophan side chain (W796) on S3 (Figure 5D). Relative to the VSD2-activated state, the S3–S4 linker is taugted (Figure 5B), and S821 approximates the location occupied by R2. Consequently, the S4 arginine side chains relocate nearly two positions along the gating charge trans-

Figure 6. Cryo-EM Structures Provide Insight into Activation Gating

(A) Intracellular view of the ProTx2-VSD2-NavAb channel in the activated (gray) state

(B) Structure of the ProTx2-VSD2-NavAb channel in the deactivated state (orange/red) superimposed with the ProTx2-VSD2-activated (gray) state.

(C) Chain A of ProTx2-VSD2-activated (gray) state with a neighboring PM in surface representation. Gating charges (blue spheres), a conserved hydrophobic constriction site phenylalanine side-chain (green sticks), and an S4–S5 linker serine side chain (yellow spheres) are shown for reference.

(D) Chain A of ProTx2-VSD2-deactivated (orange) with a neighboring PM in surface representation. Gating charges (purple spheres), a conserved hydrophobic constriction site phenylalanine side-chain (green sticks), and an S4–S5 linker serine side chain (yellow spheres) are shown for reference.

(E) Similar to (C) and (D), but as superposition and intracellular view.

(F) Similar to (D), with chain B of the ProTx2-VSD2-deactivated state (red).

See also Figures S4 and S5; Table S2; and Videos S1, S2, and S3.

fer pathway, where R2 and R3 toggle between the intracellular and extracellular vestibules. Complete or partial translocation of the R3 and R2 gating charges across the HCS, respectively, is consistent with physiological measurements and may represent the movement of 1–2 elementary charges across the membrane electric field. Overall, the details of VSD2 activation and gating charge transfer observed here are reminiscent of a sliding-helix model of voltage sensing (Figures 6C–6F) (Catterall, 1986).

Structure-Based Model of Activation Gating

Visualizing the same channel construct in VSD2-activated and deactivated states

provides remarkable insight into the mechanism of electromechanical coupling and activation gating in voltage-gated ion channels (Figures 5A, 5B, 6A, 6B, and S5D–S5E). Upon superposition of the ProTx2-VSD2-activated and ProTx2-VSD2-deactivated state structures, a number of intriguing observations are made. First, the VSDs do not pivot around the PM, implying that the VSD-PM interface may be a fulcrum that allows the S4 to perform mechanical work on the pore (Figures 6A–6D and 6F) (Lee et al., 2009). Second, the S1–S3 region undergoes a ~ 3 -Å rigid body shift to accommodate the large S4 translations (~ 10 Å) (Figure 6E), where this shift can also transport the HCS within the membrane ~ 2 Å, which may help to shape the electric field (Figures 6C and 6D) (Kintzer et al., 2018). Third, in the

VSD2-deactivated state, the S4 buckles or kinks just below the R4 gating charge, identifying an intracellular hinge between the S4 helix and S4–S5 linker that we refer to as the S4b (Figures 6D–6F). Fourth, concurrent with S4b appearance, the proximal S4–S5 linker is pushed ~ 8 Å into the cytosol and toward the PM to impinge upon the central S6 gate (Figures 6B–6F). Fifth, the S4 imparts torque as a result of kinking that imposes a $\sim 20^\circ$ rolling motion along the S4–S5 linker (Figures 6B and 6D–6F). Sixth, the S6 helices evolve from a near symmetric, dilated gate structure into a collapsed, non-conductive, asymmetric structure between the VSD2-activated and deactivated states (Figures 6A, 6B, and S5D and Video S3). In summary, the VSDs remain positioned firmly around the PM, allowing the S4 helices to deactivate and buckle, which rolls the S4–S5 linker inward to tightly close the S6 gate. This structural framework may approximate the electromechanical coupling and activation gating mechanisms operating in canonical voltage-gated ion channels.

DISCUSSION

We used protein engineering, X-ray crystallography, and cryo-EM methods to visualize structural details of ProTx2 in complex with the human Nav1.7 VSD2 receptor site. Membrane partitioning serves to concentrate ProTx2, restrict its rotation, and impose a two-dimensional receptor site search. Aromatic and basic residues cooperate to achieve membrane partitioning and receptor site engagement, where ProTx2 acts as an electrostatic modulator of VSD2. In the VSD2-activated state, ProTx2 uses R22 and K26 to target E811 and D816 (Figure 3D). In the VSD2-deactivated state, ProTx2 can additionally employ R22 to neutralize E818. The capacity of R22 and K26 to engage in sustained electrostatic interactions with E811 (K26), D816 (R22), and E818 (R22) explains why ProTx2 can target activated and deactivated states of VSD2 (Figures 2F, 5E, and 5F). These observations also justify why ProTx2 has higher affinity for the closed Nav1.7 channel and simultaneously rationalize the selectivity of ProTx2, because F813 (S3-stabilizing), E811, D816, and E818 are collectively unique to Nav1.7 (Figure S6B). Finally, ProTx2 may remain bound to VSD2 during Nav1.7 gating because the S3–S4 loop appears mobile, and the S2–S3 interface does not undergo appreciable rearrangements upon VSD2 activation.

ProTx2 functions as an electrostatic modulator of Nav1.7. The main interface between ProTx2 and VSD2 is electrostatic in nature, and toxin potency can be dramatically impacted by targeted charge neutralization (e.g., R22Q) or charge reversal (e.g., K26E) or by increasing ionic strength (Figures 4C and S6F). Importantly, we find that the E811A and D816A mutations in Nav1.7 markedly right shift channel activation (Figure 4D), an effect that mimics the action of ProTx2 itself. E811 and D816 (and to a lesser extent, E818) are therefore key extracellular acidic residues in Nav1.7 that normally catalyze the outward movement of S4 gating charges in VSD2. The S3–S4 loop in Nav1.7 VSD2 is reminiscent of a strongly acidic S3–S4 loop discovered in specialized Kv channels of electric fish that also electrostatically tunes voltage-sensor and Kv channel activation (Swapna et al., 2018). Thus, by targeting the S3–S4 loop in VSD2,

ProTx2 has uncovered an elegant way to potently and selectively induce profound gating modulation onto Nav1.7.

ProTx2 does not appear to antagonize Nav1.7 through a classic voltage-sensor trapping mechanism, since other structurally characterized gating modifiers contact S4 gating charges directly. For example, GX-936 is a small molecule antagonist that forms a direct ionic interaction with a gating charge in VSD4 to trap an activated conformation (Ahuja et al., 2015), whereas the S4 helix location in our VSD2-deactivated structure indicates that ProTx2 cannot operate through a similar mechanism (Figure 5F). Dc1a is a peptide toxin that selectively activates insect Nav channels, but unlike ProTx2, Dc1a extensively engages the S1–S2 loop, PM, and the S4 helix to lock VSD2 into an activated conformation (Shen et al., 2018). However, divalent cations can antagonize some TPC and Hv1 channels, and structures of deactivated VSD-divalent complexes have demonstrated that multipoint, transmembrane-bridging interactions are sufficient to antagonize VSD activation (Guo et al., 2016; Takeshita et al., 2014). Thus, although ProTx2 does not establish an extensive transmembrane-bridging coordination scheme, the interplay of R22 and K26 with the S3–S4 loop may serve to impede or trap the S4 helix in an analogous way.

R22 and K26 from ProTx2 invade VSD2 to impart electrostatic gating modulation onto Nav1.7 (Figures 4A–4C), where voltage-dependent properties of the channel can be altered by the side-chain chemistry inserted into the extracellular vestibule (Table S3). These findings align with charge neutralization and charge reversal studies of ENC residues that also produce depolarizing shifts in Nav channel activation (Groome and Winston, 2013; Pless et al., 2014). However, the L823R pathogenic mutation on S4 represents a natural case where the “invasion” of an extra arginine side chain into the extracellular vestibule of VSD2 produces a hyperpolarizing gain of function in Nav1.7 (Lampert et al., 2009). Therefore, L823R confirms that the precise geometry of the electrostatic gating modifier is an essential parameter for impacting Nav1.7 function (Figure 4C and Table S3), which has implications for future drug discovery efforts.

Multi-VSD targeting of ProTx2 has been previously suggested (Bosmans et al., 2008; Xiao et al., 2010, 2014); however, the lack of ProTx2 modulation on F813C-MTSET-modified channels confirms that ProTx2 does not appreciably impact other Nav1.7 VSDs at the concentrations we have tested (Figure 3G). Moreover, available VSD4 structures indicate that ProTx2 would not bind without significant rearrangements or an alternate binding mode (Figures 2C–2E) (Ahuja et al., 2015; Pan et al., 2018). Therefore, multi-VSD targeting may be more pertinent for other Nav channel subtypes or ICK toxins (Redaelli et al., 2010; Smith et al., 2007); for example, Hm-3 is a related ICK toxin that selectively targets VSD1 of Nav1.4 (Männikko et al., 2018).

Elucidating the structural basis of voltage sensing and electromechanical coupling in voltage-gated ion channels remains an important goal of basic and biomedical research (Catterall et al., 2005; Huang et al., 2017), but obtaining experimental structures of deactivated VSD states has been technically challenging. Here, the high potency and allosteric mechanism of ProTx2 has allowed us to pharmacologically trap the VSD2-NavAb channel into activated and deactivated states, and these structural snapshots reveal how the peripheral VSDs perform

mechanical work on the central PM through the S4–S5 linkers (Videos S2 and S3). Starting from the activated state, a downward ~ 10 Å translation of the S4 helix enforces a closed S6 gate through reciprocal ~ 8 Å displacements of the proximal S4–S5 linker (Figures 6A–6F). Unexpectedly, buckling or kinking at the intracellular end of the S4 helix appears to be the key molecular event that drives the S4–S5 linker to undergo large movements, and this kinking forces the S4–S5 linker to roll along the S6 helix to impact the activation gate (Figures 6D–6F). In this view of activation gating, at least one gating charge (R3) has transported completely across the HCS of VSD2 (Figure 5C), as the VSDs remain fixed alongside the PM to allow the S4 to perform electromechanical coupling to the pore (Figures 6A–6F) (Lee et al., 2009). Although Na⁺ currents have not yet been recorded for our VSD2-NavAb channel construct, the emerging structural details are reminiscent of classic models of voltage sensing and electromechanical coupling in conventional voltage-gated ion channels (Catterall, 1986; Long et al., 2007).

Our visualization of ProTx2 in complex with Nav1.7 VSD2 at high resolution reveals a small and partially lipid-exposed receptor site that establishes a critical role for membrane partitioning in high-affinity binding. ProTx2 engages in selective and durable interactions by targeting the electronegative S3–S4 loop of VSD2, whereby the toxin employs two basic side chains to neutralize key catalytic acidic residues. Thus, ProTx2 acts as an electrostatic modulator to oppose S4 movement, which, from the closed state, allosterically couples through the S4–S5 linker to impinge upon the S6 activation gate. How ProTx2 decreases conductance in addition to shifting voltage dependence of Nav1.7 will require detailed kinetic analysis of voltage-sensor movement, but it is likely due to altered VSD2 activation in the presence of toxin. In addition to providing an experimental structural framework of activation gating in canonical voltage-gated ion channels, our studies highlight new pharmacological principles that may accelerate the design of next generation Nav channel modulators.

STAR★METHODS

Detailed methods are provided in the online version of this paper and include the following:

- **KEY RESOURCES TABLE**
- **CONTACT FOR REAGENT AND RESOURCE SHARING**
- **EXPERIMENTAL MODEL AND SUBJECT DETAILS**
 - Cell Lines
- **METHOD DETAILS**
 - Recombinant expression of Nav1.7 VSD2-NavAb
 - Purification of Nav1.7 VSD2-NavAb
 - Expression and purification of recombinant ProTx2
 - Chemical synthesis of ProTx2 variants and other toxins
 - Generation of monoclonal antibodies and Fab fragments
 - ProTx2-VSD2-NavAb channel complex crystallization
 - X-ray crystallography, structure determination and refinement
 - Cryo-EM sample preparation and data acquisition
 - Cryo-EM image processing

- Cryo-EM model Building
- Automated whole cell patch clamp recordings
- **QUANTIFICATION AND STATISTICAL ANALYSIS**
 - Cryo-EM
 - Electrophysiology
- **DATA AND SOFTWARE AVAILABILITY**

SUPPLEMENTAL INFORMATION

Supplemental Information includes six figures, three tables, and three videos and can be found with this article online at <https://doi.org/10.1016/j.cell.2018.12.018>.

ACKNOWLEDGMENTS

We thank our colleagues in the Neuroscience, Structural Biology, Biochemical and Cellular Pharmacology, BioMolecular Resources, and Antibody Engineering departments for their support and in particular thank Ryan Ferrao, Yoana Dimitrova, Christian Cunningham, Si Hyun Kim, Yongmei Chen, Jim Kiefer, and Sarah Hymowitz. We thank Charlie Cohen for feedback, Dan Cawley for generating the Fab used in this study, and SmarTox Biotechnology and CPC Scientific for generating the ProTx2 derivatives. F.T. acknowledges support from the Medical Research Council (Proximity to Discovery Award, MC_PC_14128). Diffraction studies were carried out at the Stanford Synchrotron Radiation Lightsource 12-2 at Stanford Linear Accelerator Center National Accelerator Laboratory; use thereof is supported by the U.S. Department of Energy (DOE), DOE Office of Biological and Environmental Research, National Institutes of Health (NIH), and National Institute of General Medical Sciences (NIGMS). Diffraction studies were also carried out at the IMCA-CAT beamline 17-ID at the Advanced Photon Source that was supported by the companies of the Industrial Macromolecular Crystallography Association through a contract with Hauptman-Woodward Medical Research Institute; this research therefore used resources of the Advanced Photon Source, a U.S. Department of Energy (DOE) Office of Science User Facility operated for the DOE Office of Science by Argonne National Laboratory under Contract No. DE-AC02-06CH11357. Reagents are available under a materials transfer agreement with Genentech.

AUTHOR CONTRIBUTIONS

H.X. established conditions for purification, complex formation, and crystallization of the ProTx2-VSD2-NavAb channel. F.T. assisted in sample preparation and crystallization. E.W., C.K., and Y.F. provided molecular biology and expression support. H.X. and J.P. determined, refined, and analyzed the crystal structure. H.X. characterized the Fab and formed complexes with the ProTx2-VSD2-NavAb channel. H.X., A.E., and C.P.A. established conditions for cryo-EM sample preparation. H.X., C.P.A., A.R., and C.C. established conditions for cryo-EM data collection and processing. H.X. and A.R. analyzed the cryo-EM data and structures. T.L. and D.H.H. performed electrophysiological studies with support from J.C. H.X., T.L., A.R., D.H.H., C.M.K. and J.P. prepared the manuscript with input from all other authors. T.L., A.R., D.H.H., C.M.K., and J.P. are co-senior authors, and J.P. and C.M.K. supervised the project.

DECLARATION OF INTERESTS

All authors are/were Genentech employees. T.L., A.R., C.P.A., E.W., A.E., C.K., Y.F., J.C., C.C., D.H.H., C.M.K., and J.P. hold shares in the Genentech/Roche group.

Received: July 2, 2018

Revised: September 11, 2018

Accepted: December 11, 2018

Published: January 17, 2019; corrected online: January 18, 2019

REFERENCES

- Adams, P.D., Afonine, P.V., Bunkóczi, G., Chen, V.B., Davis, I.W., Echols, N., Headd, J.J., Hung, L.W., Kapral, G.J., Grosse-Kunstleve, R.W., et al. (2010). PHENIX: a comprehensive Python-based system for macromolecular structure solution. *Acta Crystallogr. D Biol. Crystallogr.* **66**, 213–221.
- Ahuja, S., Mukund, S., Deng, L., Khakh, K., Chang, E., Ho, H., Shriver, S., Young, C., Lin, S., Johnson, J.P., Jr., et al. (2015). Structural basis of Nav1.7 inhibition by an isoform-selective small-molecule antagonist. *Science* **350**, aac5464.
- Bezanilla, F. (2018). Gating currents. *J. Gen. Physiol.* **150**, 911–932.
- Bosmans, F., Martin-Eauclaire, M.F., and Swartz, K.J. (2008). Deconstructing voltage sensor function and pharmacology in sodium channels. *Nature* **456**, 202–208.
- Campos, F.V., Chanda, B., Beirão, P.S., and Bezanilla, F. (2008). Alpha-scorpion toxin impairs a conformational change that leads to fast inactivation of muscle sodium channels. *J. Gen. Physiol.* **132**, 251–263.
- Capes, D.L., Goldschen-Ohm, M.P., Arcisio-Miranda, M., Bezanilla, F., and Chanda, B. (2013). Domain IV voltage-sensor movement is both sufficient and rate limiting for fast inactivation in sodium channels. *J. Gen. Physiol.* **142**, 101–112.
- Cardone, G., Heymann, J.B., and Steven, A.C. (2013). One number does not fit all: mapping local variations in resolution in cryo-EM reconstructions. *J. Struct. Biol.* **184**, 226–236.
- Catterall, W.A. (1986). Molecular properties of voltage-sensitive sodium channels. *Annu. Rev. Biochem.* **55**, 953–985.
- Catterall, W.A., Goldin, A.L., and Waxman, S.G. (2005). International Union of Pharmacology. XLVII. Nomenclature and structure-function relationships of voltage-gated sodium channels. *Pharmacol. Rev.* **57**, 397–409.
- Cestèle, S., Qu, Y., Rogers, J.C., Rochat, H., Scheuer, T., and Catterall, W.A. (1998). Voltage sensor-trapping: enhanced activation of sodium channels by beta-scorpion toxin bound to the S3-S4 loop in domain II. *Neuron* **21**, 919–931.
- Chanda, B., and Bezanilla, F. (2002). Tracking voltage-dependent conformational changes in skeletal muscle sodium channel during activation. *J. Gen. Physiol.* **120**, 629–645.
- Chen, V.B., Arendall, W.B., 3rd, Headd, J.J., Keedy, D.A., Immormino, R.M., Kapral, G.J., Murray, L.W., Richardson, J.S., and Richardson, D.C. (2010). MolProbity: all-atom structure validation for macromolecular crystallography. *Acta Crystallogr. D Biol. Crystallogr.* **66**, 12–21.
- Cronin, C.N., Lim, K.B., and Rogers, J. (2007). Production of selenomethionyl-derivatized proteins in baculovirus-infected insect cells. *Protein Sci.* **16**, 2023–2029.
- Dib-Hajj, S.D., Cummins, T.R., Black, J.A., and Waxman, S.G. (2007). From genes to pain: Na^v 1.7 and human pain disorders. *Trends Neurosci.* **30**, 555–563.
- Emsley, P., and Cowtan, K. (2004). Coot: model-building tools for molecular graphics. *Acta Crystallogr. D Biol. Crystallogr.* **60**, 2126–2132.
- Flinspach, M., Xu, Q., Piekarczyk, A.D., Fellows, R., Hagan, R., Gibbs, A., Liu, Y., Neff, R.A., Freedman, J., Eckert, W.A., et al. (2017). Insensitivity to pain induced by a potent selective closed-state Nav1.7 inhibitor. *Sci. Rep.* **7**, 39662.
- Gao, Y., Cao, E., Julius, D., and Cheng, Y. (2016). TRPV1 structures in nanodiscs reveal mechanisms of ligand and lipid action. *Nature* **534**, 347–351.
- Gilchrist, J., Olivera, B.M., and Bosmans, F. (2014). Animal toxins influence voltage-gated sodium channel function. *Handb. Exp. Pharmacol.* **227**, 203–229.
- Grant, T., Rohou, A., and Grigorieff, N. (2018). cisTEM, user-friendly software for single-particle image processing. *eLife* **7**.
- Groome, J.R., and Winston, V. (2013). S1-S3 counter charges in the voltage sensor module of a mammalian sodium channel regulate fast inactivation. *J. Gen. Physiol.* **141**, 601–618.
- Guo, J., Zeng, W., Chen, Q., Lee, C., Chen, L., Yang, Y., Cang, C., Ren, D., and Jiang, Y. (2016). Structure of the voltage-gated two-pore channel TPC1 from *Arabidopsis thaliana*. *Nature* **531**, 196–201.
- Henriques, S.T., Deplazes, E., Lawrence, N., Cheneval, O., Chausis, S., In-serra, M., Thongyoo, P., King, G.F., Mark, A.E., Vetter, I., et al. (2016). Interaction of Tarantula Venom Peptide ProTx-II with Lipid Membranes Is a Prerequisite for Its Inhibition of Human Voltage-gated Sodium Channel Nav1.7. *J. Biol. Chem.* **291**, 17049–17065.
- Huang, W., Liu, M., Yan, S.F., and Yan, N. (2017). Structure-based assessment of disease-related mutations in human voltage-gated sodium channels. *Protein Cell* **8**, 401–438.
- Kabsch, W. (2010). Xds. *Acta Crystallogr. D Biol. Crystallogr.* **66**, 125–132.
- Kintzer, A.F., Green, E.M., Dominik, P.K., Bridges, M., Armache, J.P., Deneka, D., Kim, S.S., Hubbell, W., Kossiakoff, A.A., Cheng, Y., and Stroud, R.M. (2018). Structural basis for activation of voltage sensor domains in an ion channel TPC1. *Proc. Natl. Acad. Sci. USA* **115**, E9095–E9104.
- Lampert, A., Dib-Hajj, S.D., Eastman, E.M., Tyrrell, L., Lin, Z., Yang, Y., and Waxman, S.G. (2009). Erythromelalgia mutation L823R shifts activation and inactivation of threshold sodium channel Nav1.7 to hyperpolarized potentials. *Biochem. Biophys. Res. Commun.* **390**, 319–324.
- Lee, S.Y., and MacKinnon, R. (2004). A membrane-access mechanism of ion channel inhibition by voltage sensor toxins from spider venom. *Nature* **430**, 232–235.
- Lee, S.Y., Banerjee, A., and MacKinnon, R. (2009). Two separate interfaces between the voltage sensor and pore are required for the function of voltage-dependent K⁽⁺⁾ channels. *PLoS Biol.* **7**, e47.
- Lee, S.C., Bennett, B.C., Hong, W.X., Fu, Y., Baker, K.A., Marcoux, J., Robinson, C.V., Ward, A.B., Halpert, J.R., Stevens, R.C., et al. (2013). Steroid-based facial amphiphiles for stabilization and crystallization of membrane proteins. *Proc. Natl. Acad. Sci. USA* **110**, E1203–E1211.
- Li, Q., Wanderling, S., Paduch, M., Medovoy, D., Singharoy, A., McGreevy, R., Villalba-Galea, C.A., Hulse, R.E., Roux, B., Schulten, K., et al. (2014). Structural mechanism of voltage-dependent gating in an isolated voltage-sensing domain. *Nat. Struct. Mol. Biol.* **21**, 244–252.
- Long, S.B., Tao, X., Campbell, E.B., and MacKinnon, R. (2007). Atomic structure of a voltage-dependent K⁽⁺⁾ channel in a lipid membrane-like environment. *Nature* **450**, 376–382.
- Männikkö, R., Shenkarev, Z.O., Thor, M.G., Berkut, A.A., Myshkin, M.Y., Paramonov, A.S., Kulbatskii, D.S., Kuzmin, D.A., Sampedro Castañeda, M., King, L., et al. (2018). Spider toxin inhibits gating pore currents underlying periodic paralysis. *Proc. Natl. Acad. Sci. USA* **115**, 4495–4500.
- Mastrorade, D.N. (2005). Automated electron microscope tomography using robust prediction of specimen movements. *J. Struct. Biol.* **152**, 36–51.
- McKerrall, S.J., and Sutherlin, D.P. (2018). Na_v1.7 inhibitors for the treatment of chronic pain. *Bioorg. Med. Chem. Lett.* **28**, 3141–3149.
- Middleton, R.E., Warren, V.A., Kraus, R.L., Hwang, J.C., Liu, C.J., Dai, G., Brochu, R.M., Kohler, M.G., Gao, Y.D., Garsky, V.M., et al. (2002). Two tarantula peptides inhibit activation of multiple sodium channels. *Biochemistry* **41**, 14734–14747.
- Mihalescu, M., Krepiy, D., Milescu, M., Gawrisch, K., Swartz, K.J., and White, S. (2014). Structural interactions of a voltage sensor toxin with lipid membranes. *Proc. Natl. Acad. Sci. USA* **111**, E5463–E5470.
- Milescu, M., Bosmans, F., Lee, S., Alabi, A.A., Kim, J.I., and Swartz, K.J. (2009). Interactions between lipids and voltage sensor paddles detected with tarantula toxins. *Nat. Struct. Mol. Biol.* **16**, 1080–1085.
- Muroi, Y., Arcisio-Miranda, M., Chowdhury, S., and Chanda, B. (2010). Molecular determinants of coupling between the domain III voltage sensor and pore of a sodium channel. *Nat. Struct. Mol. Biol.* **17**, 230–237.
- Pan, X., Li, Z., Zhou, Q., Shen, H., Wu, K., Huang, X., Chen, J., Zhang, J., Zhu, X., Lei, J., et al. (2018). Structure of the human voltage-gated sodium channel Na_v1.4 in complex with β1. *Science* **362**, aau2486.
- Park, J.H., Carlin, K.P., Wu, G., Ilyin, V.I., Musza, L.L., Blake, P.R., and Kyle, D.J. (2014). Studies examining the relationship between the chemical structure

- of protoxin II and its activity on voltage gated sodium channels. *J. Med. Chem.* **57**, 6623–6631.
- Payandeh, J., and Hackos, D.H. (2018). Selective Ligands and Drug Discovery Targeting the Voltage-Gated Sodium Channel Nav1.7. *Handb. Exp. Pharmacol.* **246**, 271–306.
- Payandeh, J., Scheuer, T., Zheng, N., and Catterall, W.A. (2011). The crystal structure of a voltage-gated sodium channel. *Nature* **475**, 353–358.
- Pettersen, E.F., Goddard, T.D., Huang, C.C., Couch, G.S., Greenblatt, D.M., Meng, E.C., and Ferrin, T.E. (2004). UCSF Chimera—a visualization system for exploratory research and analysis. *J. Comput. Chem.* **25**, 1605–1612.
- Phillips, L.R., Milesu, M., Li-Smerin, Y., Mindell, J.A., Kim, J.I., and Swartz, K.J. (2005). Voltage-sensor activation with a tarantula toxin as cargo. *Nature* **436**, 857–860.
- Pless, S.A., Elstone, F.D., Niciforovic, A.P., Galpin, J.D., Yang, R., Kurata, H.T., and Ahern, C.A. (2014). Asymmetric functional contributions of acidic and aromatic side chains in sodium channel voltage-sensor domains. *J. Gen. Physiol.* **143**, 645–656.
- Redaelli, E., Cassulini, R.R., Silva, D.F., Clement, H., Schiavon, E., Zamudio, F.Z., Odell, G., Arcangeli, A., Clare, J.J., Alagón, A., et al. (2010). Target promiscuity and heterogeneous effects of tarantula venom peptides affecting Na⁺ and K⁺ ion channels. *J. Biol. Chem.* **285**, 4130–4142.
- Richards, K.L., Milligan, C.J., Richardson, R.J., Jancovski, N., Grunnet, M., Jacobson, L.H., Undheim, E.A.B., Mobli, M., Chow, C.Y., Herzig, V., et al. (2018). Selective Nav1.1 activation rescues Dravet syndrome mice from seizures and premature death. *Proc. Natl. Acad. Sci. USA* **115**, E8077–E8085.
- Rosenthal, P.B., and Henderson, R. (2003). Optimal determination of particle orientation, absolute hand, and contrast loss in single-particle electron cryomicroscopy. *J. Mol. Biol.* **333**, 721–745.
- Schmalhofer, W.A., Calhoun, J., Burrows, R., Bailey, T., Kohler, M.G., Weinglass, A.B., Kaczorowski, G.J., Garcia, M.L., Koltzenburg, M., and Priest, B.T. (2008). ProTx-II, a selective inhibitor of Nav1.7 sodium channels, blocks action potential propagation in nociceptors. *Mol. Pharmacol.* **74**, 1476–1484.
- Schrödinger, L. (2017). PyMOL. <https://pymol.org/2/>.
- Shen, H., Li, Z., Jiang, Y., Pan, X., Wu, J., Cristofori-Armstrong, B., Smith, J.J., Chin, Y.K.Y., Lei, J., Zhou, Q., et al. (2018). Structural basis for the modulation of voltage-gated sodium channels by animal toxins. *Science* **362**, aau2596.
- Smith, J.J., Cummins, T.R., Alphy, S., and Blumenthal, K.M. (2007). Molecular interactions of the gating modifier toxin ProTx-II with Nav 1.5: implied existence of a novel toxin binding site coupled to activation. *J. Biol. Chem.* **282**, 12687–12697.
- Sokolov, S., Kraus, R.L., Scheuer, T., and Catterall, W.A. (2008). Inhibition of sodium channel gating by trapping the domain II voltage sensor with protoxin II. *Mol. Pharmacol.* **73**, 1020–1028.
- Strong, M., Sawaya, M.R., Wang, S., Phillips, M., Cascio, D., and Eisenberg, D. (2006). Toward the structural genomics of complexes: crystal structure of a PE/PPE protein complex from *Mycobacterium tuberculosis*. *Proc. Natl. Acad. Sci. USA* **103**, 8060–8065.
- Swapna, I., Ghezzi, A., York, J.M., Markham, M.R., Halling, D.B., Lu, Y., Gallant, J.R., and Zakon, H.H. (2018). Electrostatic Tuning of a Potassium Channel in Electric Fish. *Curr. Biol.* **28**, 2094–2102.
- Swartz, K.J., and MacKinnon, R. (1997). Hanatoxin modifies the gating of a voltage-dependent K⁺ channel through multiple binding sites. *Neuron* **18**, 665–673.
- Takeshita, K., Sakata, S., Yamashita, E., Fujiwara, Y., Kawanabe, A., Kurokawa, T., Okochi, Y., Matsuda, M., Narita, H., Okamura, Y., and Nakagawa, A. (2014). X-ray crystal structure of voltage-gated proton channel. *Nat. Struct. Mol. Biol.* **21**, 352–357.
- Tang, G., Peng, L., Baldwin, P.R., Mann, D.S., Jiang, W., Rees, I., and Ludtke, S.J. (2007). EMAN2: an extensible image processing suite for electron microscopy. *J. Struct. Biol.* **157**, 38–46.
- Tao, X., Lee, A., Limapichat, W., Dougherty, D.A., and MacKinnon, R. (2010). A gating charge transfer center in voltage sensors. *Science* **328**, 67–73.
- Urzhumtsev, A., Afonine, P.V., and Adams, P.D. (2013). TLS from fundamentals to practice. *Crystallogr. Rev.* **19**, 230–270.
- Wright, Z.V.F., McCarthy, S., Dickman, R., Reyes, F.E., Sanchez-Martinez, S., Cryar, A., Kilford, I., Hall, A., Takle, A.K., Topf, M., et al. (2017). The Role of Disulfide Bond Replacements in Analogues of the Tarantula Toxin ProTx-II and Their Effects on Inhibition of the Voltage-Gated Sodium Ion Channel Nav1.7. *J. Am. Chem. Soc.* **139**, 13063–13075.
- Xiao, Y., Blumenthal, K., Jackson, J.O., 2nd, Liang, S., and Cummins, T.R. (2010). The tarantula toxins ProTx-II and huwentoxin-IV differentially interact with human Nav1.7 voltage sensors to inhibit channel activation and inactivation. *Mol. Pharmacol.* **78**, 1124–1134.
- Xiao, Y., Blumenthal, K., and Cummins, T.R. (2014). Gating-pore currents demonstrate selective and specific modulation of individual sodium channel voltage-sensors by biological toxins. *Mol. Pharmacol.* **86**, 159–167.

STAR★METHODS

KEY RESOURCES TABLE

REAGENT or RESOURCE	SOURCE	IDENTIFIER
Antibodies		
Mouse monoclonal anti-NavAb antibody	This paper	7A9
Chemicals, Peptides, and Recombinant Proteins		
Ham's F-12	ThermoFisher Scientific	Cat# 31765035
Tet System Approved fetal bovine serum	Clontech	Cat# 631106
DMEM (Dulbecco's modified Eagle's medium)	ThermoFisher Scientific	Cat# 10569010
GlutaMAX TM supplement	ThermoFisher Scientific	Cat# 35050061
Accutase	Innovative Cell Technologies	Cat# AT104-500
CHO-S-SFM II medium	ThermoFisher Scientific	Cat# 31033020
MTSEA	Toronto Research Chemicals	Cat# A609150
MTSET	Toronto Research Chemicals	Cat# T795903
MTSES	Toronto Research Chemicals	Cat# S672000
Tetrodotoxin (TTX)	ThermoFisher Scientific	Cat# 50-753-2807
Lipofectamine 2000 Transfection Reagent	Invitrogen	Cat# 11668019
ESF 921 Insect Cell Culture Medium	Expression Systems	Cat# 96-001-01
cOmplete EDTA-free protease-inhibitor cocktail tablets	Roche	Cat# 11873580001
Ni-NTA agarose	QIAGEN	Cat# 30210
ANTI-FLAG M2 Affinity Gel	Sigma-Aldrich	Cat# A2220
FLAG Peptide	Sigma-Aldrich	Cat# F3290
GDN	Anatrace	Cat# GDN101
Facade-EM	Avanti Polar Lipids	Cat# 850522
1-palmitoyl-2-oleoyl-glycerol-3-phosphocholine (POPC)	Avanti Polar Lipids	Cat# 850457
1-palmitoyl-2-oleoyl-sn-glycerol-3-phosphoethanolamine (POPE)	Avanti Polar Lipids	Cat# 850757
1-palmitoyl-2-oleoyl-sn-glycerol-3-phospho-(1'-rac-glycerol) (POPG)	Avanti Polar Lipids	Cat# 840457
Brain Polar Lipid Extract (Porcine)	Avanti Polar Lipids	Cat# 141101
Pierce Fab Preparation Kit	Thermo scientific	Cat# 44985
ProTx2	Alomone Labs	Cat# STP-100
ProTx2	Smartox Biotechnology	Cat# 07PTX002-00100
ProTx2 variants	Smartox Biotechnology	N/A
ProTx2 (SeCys-substituted)	CPC Scientific	N/A
GrTx1	Alomone Labs	Cat# STG-250
GrTx1	Smartox Biotechnology	Cat# GRX
GrTx1 variants	Smartox Biotechnology	N/A
GsAf1	Alomone Labs	Cat# STG-300
GsAf2	Alomone Labs	Cat# STG-350
PaTx1	Alomone Labs	Cat# STP-700
Deposited Data		
Crystal structure of Nav1.7 VSD2-ProTx2	This paper	PDB: 6N4I
Nav1.7 VSD2-ProTx2 (activated state) atomic model and density map	This paper	PDB: 6N4Q EMDB: EMD-0341
Nav1.7 VSD2-ProTx2 (deactivated state) atomic model and density map	This paper	PDB: 6N4R EMDB: EMD-0342

(Continued on next page)

Continued

REAGENT or RESOURCE	SOURCE	IDENTIFIER
Experimental Models: Cell Lines		
Human: HEK293 Nav1.1 cells, Tetracycline-inducible	Xenon Pharma	N/A
Human: HEK293 Nav1.2 cells, Tetracycline-inducible	Xenon Pharma	N/A
Hamster: CHO Nav1.3 cells, Tetracycline-inducible	ChanTest	Cat# CT6157
Human: HEK293 Nav1.4 cells, constitutive	ChanTest	Cat# CT6005
Hamster: CHL Nav1.5 cells, constitutive	Genentech	N/A
Human: HEK293 Nav1.6 cells, Tetracycline-inducible	Xenon	N/A
Hamster: CHO stable cell lines expressing wild type or mutant Nav1.7 channels	Genentech, this paper	N/A
Tni (<i>Trichoplusia ni</i>) insect cells	Expression Systems	Cat# 94-002F
Recombinant DNA		
pBiCMV containing human SCN2B	This paper	N/A
His-MBP-ProTx2	This paper	DNA770148
Nav1.7 VSD2-NavAb chimera	This paper	DNA766564
Software and Algorithms		
PatchController384 (version 1.5.2)	Nanion Technologies	https://www.nanion.de/en/products/syncropatch-384pe.html
DataController384 (version 1.5.0)	Nanion Technologies	https://www.nanion.de/en/products/syncropatch-384pe.html
PatchMaster (version 2.90)	HEKA Elektronik	https://www.heka.com/products/products_main.html#soft_pm
FitMaster (version 2.90)	HEKA Elektronik	https://www.heka.com/products/products_main.html#soft_fit
Prism (version 6.05)	Graphpad	https://www.graphpad.com/scientific-software/prism/
XDS	Kabsch, 2010	http://xds.mpimf-heidelberg.mpg.de/
UCLA Diffraction Anisotropy Server	Strong et al., 2006	http://services.mbi.ucla.edu/anisoscale
PHENIX	Adams et al., 2010	https://www.phenix-online.org
Molprobrity	Chen et al., 2010	http://molprobrity.biochem.duke.edu
SerialEM	Mastrorade, 2005	http://bio3d.colorado.edu/SerialEM
cisTEM	Grant et al., 2018	https://cistem.org/
EMAN2	Tang et al., 2007	https://blake.bcm.edu/emanwiki/EMAN2
Coot	Emsley and Cowtan, 2004	http://www2.mrc-lmb.cam.ac.uk/Personal/pemsley/cool/
UCSF Chimera	Pettersen et al., 2004	http://www.cgl.ucsf.edu/chimera/
PyMOL	Schrödinger, 2017	https://pymol.org/2/
Other		
SyncroPatch 768PE	Nanion Technologies	https://www.nanion.de/en/products/syncropatch-384pe.html
EPC-10 amplifier	HEKA Elektronik	https://www.heka.com/products/products_main.html#physiol_epc10single
HiTrap MabSelect SuRe column	GE Healthcare	Cat# 11003494
Superdex 200 Increase 10/300 GL column	GE Healthcare	Cat# 28990944
Superdex 75 Increase 10/300 GL column	GE Healthcare	Cat# 29148721
Superose 6 Increase 3.2/300 column	GE Healthcare	Cat# 29091598
Superose 6 Increase 10/300 GL column	GE Healthcare	Cat# 29091596
200 mesh CF-1.2/1.3-2C C-flat holey carbon grids	Electron Microscopy Sciences	Cat# CF213

CONTACT FOR REAGENT AND RESOURCE SHARING

Further information and requests for reagents should be directed to and will be fulfilled by the Lead Contact, Jian Payandeh (payandeh.jian@gene.com).

EXPERIMENTAL MODEL AND SUBJECT DETAILS

Cell Lines

Tri (*Trichoplusia ni*) insect cells were used for protein expression and maintained in ESF 921 insect cell culture medium at 27°C. These cells are female in origin.

For electrophysiological recordings, the human Nav expression cell lines and cDNA constructs used were as follows: Tetracycline-inducible HEK293 cell lines: Nav1.1, Nav1.2 and Nav1.6 (Xenon, Canada); Tetracycline-inducible CHO cell line: Nav1.3 (ChanTest, Ohio); HEK293 cell lines: Nav1.4 (ChanTest, Ohio), CHO Nav1.7 (Anaxon, Switzerland); CHL cell lines: Nav1.5 (Genentech in-house). These cells are female in origin. Full length human Nav channel cDNA clones Nav1.7 (XM_011511618) and Nav1.2 (NM_021007) were assembled (Genescript) based on published wide type and desired mutation sequences, and were cloned into mammalian expression vectors: pBiCMV containing the human $\beta 2$ accessory subunit. Transient transfections were performed with Lipofectamine 2000 (Invitrogen). Stable cell lines expressing mutant Nav1.7 channels were generated for use in automated patch clamp experiments as per manufacturer's instructions (Clontech). All cell culture reagents were obtained from Invitrogen. Cell lines were cultured in basal medium, high glucose DMEM (for HEK293 and CHL host cells) or Ham's F12 for (CHO host cell), supplemented with 10% FBS, 2 mM L-Glutamine and required selection antibiotic in 5% CO₂ at 37°C.

METHOD DETAILS

Recombinant expression of Nav1.7 VSD2-NavAb

The human Nav1.7 VSD2-NavAb channel chimera constructs were synthesized (Genescript) and cloned into a modified pAcGP67A vector downstream of the polyhedron promoter and an N-terminal Flag-tag. Recombinant baculovirus was generated using the Baculogold system (BD Biosciences) following standard protocols. *Trichoplusia ni* cells were infected for protein production and harvested 48 hr post-infection. Selenomethionine (SeMet) incorporated VSD2-NavAb protein was expressed using standard labeling protocols (Cronin et al., 2007). Sequence of the crystallization construct is:

MDYKDDDDKGSLVPRGSHMYLRITNIVESSFFTKFIYLIVLNTLFMAMEHHPMTEEFKNVLAIGNLVFTGIFAIEILRIYVHRISFFKDPW
SLFDLIVTL~~SLVELFLADVEGLSVLR~~SFRLLRVFRLVTAVPQMRKIVSALISVIPGMLSVIALMTLFFYIFAIMATQLFGERFPWFVGTGLESF
YTLFQVMTLESWSMGIVRPLMEVYPYAWVFFIPFIFVTFVMINLVVAICVDAMAILNQKEEQHIIDEVQSHEDNINNEI~~IKLREEIVELKELIK~~
TSLKN.

The underlined sequence is the FLAG affinity tag and thrombin protease cleavage site.

Purification of Nav1.7 VSD2-NavAb

Trichoplusia ni cells expressing VSD2-NavAb channels were resuspended in 50 mM Tris pH 8.0, 200 mM NaCl (Buffer A) supplemented with cOmplete EDTA-free protease-inhibitor cocktail tablets (Roche). Cell suspension was passed through a microfluidizer twice at a pressure setting of 15,000 psi. Following cell lysis, 1% (w/v) GDN (Anatrace) was added and solubilization was carried out with gentle agitation for 2 hr at 4°C. After ultracentrifugation at 100,000 x g at 4°C for 1 hr, clarified supernatant was mixed gently with anti-Flag M2-agarose resin (Sigma) pre-equilibrated with Buffer B (50 mM Tris pH 8.0, 200 mM NaCl, 0.042% GDN) for 2.5 hr at 4°C. Flag resin was collected by gravity flow and washed with 5 column volumes of Buffer B. Flag-tagged VSD2-NavAb was eluted with Buffer C (50 mM Tris pH 8.0, 200 mM NaCl, 0.06% FA3 (Avanti), 0.1 mg/mL POPC:POPE:POPG (Avanti) mixed at molar ratio 3:1:1 and 0.15 mg/mL Flag peptide. Eluate was passed over a Superose 6 Increase 10/300 GL column (GE Healthcare) in Buffer D (10 mM Tris pH 8.0, 100 mM NaCl, 0.06% FA3, 0.1 mg/mL POPC:POPE:POPG mixed at molar ratio 3:1:1), and peak fractions were concentrated to ~25 mg/mL using a Amicon Ultra-15 Centrifugal Filter Units (100K MWCO, Millipore Sigma).

Expression and purification of recombinant ProTx2

A ProTx2 construct was synthesized (Genescript) and cloned into a modified pAcGP67A vector downstream of the polyhedron promoter, a signal sequence, an N-terminal His-tag, an N-terminal maltose binding protein (MBP) fusion, and a TEV cleavage site (His-MBP-ProTx2); and recombinant baculovirus was generated using the Baculogold system (BD Biosciences) following standard protocols. His-MBP-ProTx2 was expressed in *Trichoplusia ni* cells for 48 hr as a secreted protein to facilitate disulfide bond formation and SeMet incorporated His-MBP-ProTx2 was expressed using standard labeling protocols (Cronin et al., 2007). In brief, healthy dividing insect cells at high viability (> 98%) and at densities of ~4 × 10⁶ cells/mL were split into ESF-921 protein-free methionine-free medium with SeMet 100 mg/L and allowed to grow for 24 hr. These cells were used to inoculate a 10 L wave bag to a density of 2 × 10⁶ cells/mL in the same media; the cells were infected at a multiplicity of infection of 1 and harvested 48 hr post infection. After cells were pelleted, cell culture supernatant was mixed gently with 50 mM Tris pH 8.0, 5 mM CaCl₂ and 1 mM NiCl₂ for 15 min and then centrifuged at 5,000 rpm for 15 min. Supernatant was filtered through a 0.45 μm filter before incubation with pre-equilibrated Ni-NTA

agarose at 4°C overnight. Ni-NTA resin was collected by gravity flow, washed with 5 column volumes of Buffer E (50 mM Tris pH 8.0, 10 mM imidazole, 0.3 M NaCl). His-MBP-ProTx-II was eluted with 50 mM Tris pH 7.5, 250 mM imidazole, 0.15 M NaCl and passed over a Superdex200 Increase 10/300 GL column (GE Healthcare). Peak fractions were treated with TEV protease and then purified by a Superdex75 Increase 10/300 GL column (GE Healthcare). Sequence of the secreted crystallization construct prior to TEV cleavage is:

```
>AGSMHHHHHHHHGKIEEGKLVIIWINGDKGYNGLAEVGGKFEKDTGIKVTVEHPDKLEEKFPQVAATGDGPDIIFWAHDRFGGYAQS
GLLAEITPKAFQDKLYPFTWDAVRYNGKLIAYPIAVEALSLIYNKDLLPNPPKTWEEIPALDKELKAKGKSALMFNLQEPYFTWPLIAADG
GYAFKYENKDYDKVDNAGAKAGLTFVLDLIKHKHMNADTDYSIAEAFNKGETAMTINGPWAWNSNIDTSKVNYGVTVLPTFKGQP
SKPFVGVLSAGINAASPNKELAKEFLENYLLTDEGLEAVNKDKPLGAVALKSYEEELAKDPRIAATMENAQKGEIMPNIQMSAFWYAVR
TAVINAASGRQTVDEALKDAQTNSSNNNNNNNNNGENLYFQGGDDDKYCQKWMWTCDSERKCCEGMVCRLLWCKKKLW.
```

The underlined sequence is the TEV protease cleavage site.

Chemical synthesis of ProTx2 variants and other toxins

Wild-type ProTx2 and GrTx1 were purchased from Alomone Labs and Smartox Biotechnology (France). ProTx2 and GrTx1 variants were synthesized by Smartox Biotechnology (France). SeCys-substituted ProTx2 was synthesized by CPC Scientific. For crystallization, ProTx2 (wild-type or SeCys derivatives) was resuspended in 20 mM HEPES pH 7.0, 100 mM NaCl to make 1 mM stock. For electrophysiological studies, toxins were resuspended directly in extracellular recording solution.

Generation of monoclonal antibodies and Fab fragments

The monoclonal antibody (mAb) against VSD2-NavAb was raised using standard methods. Hybridomas were generated by immunization of mice with VSD2-NavAb reconstituted in brain polar lipid extract (porcine, Avanti) liposomes. The mAb was purified from hybridoma cell supernatant by protein A affinity chromatography and the Fab was generated by papain cleavage using Pierce Fab Preparation Kit (Thermo scientific). Fab was purified using a HiTrap MabSelect SuRe column (GE Healthcare) followed by a Superdex 75 Increase 10/300 GL column (GE Healthcare). Cloning and sequencing of Fab heavy and light chain genes were performed from mouse hybridoma cells.

ProTx2-VSD2-NavAb channel complex crystallization

Purified VSD2-NavAb was mixed with ProTx2 at 1:2 molar ratio to a final concentration of 12 mg/mL and incubated on ice for 1 hr. Protein sample was mixed in 1:1 ratio with mother liquor and set up in a sitting-drop vapor-diffusion format. Crystals appeared in conditions with well solutions containing 2.3–2.6 M ammonium sulfate, 100 mM buffer pH 4.6–7.5 at 4–19°C. The native, SeMet-substituted and SeCys-substituted protein complexes all crystallized under similar conditions. For cryoprotection, crystals were passed through a reservoir solution containing 30% (w/v) sucrose in increments of 5% sucrose prior to flash freezing in liquid nitrogen. Crystals were maintained at 100K during all data collection procedures.

X-ray crystallography, structure determination and refinement

Over 1,000 crystals were screened and nearly 100 diffraction datasets were collected at the Stanford Synchrotron Radiation Light source on beamline 12-2 and the Advanced Photon Source on beamline 17-ID (IMCA-CAT). X-ray diffraction data were integrated and scaled using XDS (Kabsch, 2010) and XSCALE. Inclusion of the highest resolution data bins was judged based on the resulting quality of electron density maps, where R_{merge} statistics are within the expected range for I/σ , $CC_{1/2}$ and CC^* statistics. For native ProTx2-VSD2-NavAb, the four highest resolution and isomorphous datasets were merged in XSCALE and corrected for anisotropic diffraction using the UCLA Diffraction Anisotropy Server (<http://services.mbi.ucla.edu/anisotropy>), where treatment of the data through the anisotropy server significantly improved the resulting electron density maps (Strong et al., 2006); similarly, merging of these four native datasets also positively impacted map features and quality. The structure was determined using PHENIX (Adams et al., 2010) by molecular replacement using coordinates of the pore module from a VSD4-NavAb crystal structure (PDB: 5EK0). Iterative rounds of refinement and model building were performed in Coot (Emsley and Cowtan, 2004) with inspection of omit and simulated annealing (SA)-omit maps. Non-crystallographic symmetry (NCS) and secondary structure restraints were used initially with group B-factor refinement. Toward later stages of refinement, individual B-factors and TLS parameters were applied (Urzhumtsev et al., 2013), with the latter noticeably improving map quality and R_{free} . The SeMet-substituted and SeCys-substituted crystal datasets collected near the Se absorption edge diffracted X-rays to $\sim 4\text{--}6$ Å with significant anomalous signal extending below 7 Å. Anomalous difference maps were generated in phenix.refine and used to identify SeMet and SeCys residues to facilitate building and refinement of the model at early and appropriate stages. For the SeMet-VSD2-NavAb derivative, SeMet peak signals were nearly equivalent across all four channel subunits within the asymmetric unit (chains A–D); for the SeMet-ProTx2 derivative, SeMet peaks from the toxin were most pronounced for chain G (associated with chain C of the channel); for the SeCys-ProTx2 derivative, SeCys peaks from the toxin were most pronounced for chain H and chain G (associated with chains D and C of the channel, respectively); although consistent across all chains of the structure, differences in anomalous peak strength may arise from the local crystal packing environment. Mid-way through refinement, phospholipids were assigned and modeled into electron density features that were consistently observed across multiple datasets and calculations. Similarly, following the modeling of lipids, ProTx2 was initially placed based on available extra density, anomalous difference maps, and the high-resolution crystal structure previously determined

(PDB: 500U). Imposing this high resolution ProTx2 structure as a reference model restraint was examined but not productive. Overall scaling statistics, refinement statistics and map quality were best determined in the C2 space group. Electron density for the S3-S4 loops remained weak in all four subunits of the channel (chains A-D) at all stages of refinement, but S3-S4 loop density was best resolved for chains A and C. The geometry of the final refined ProTx2-VSD2-NavAb model was assessed by Molprobrity (Chen et al., 2010) and high quality metrics returned. Further attempts to improve the geometry and/or clashscore resulted in significant increases in the R_{free} , therefore we consider model building and refinement to be well explored. All X-ray structural figures were rendered with PyMol (Schrödinger, 2017).

Cryo-EM sample preparation and data acquisition

Purified VSD2-NavAb was mixed with ProTx2 and Fab at 1:2:1.2 molar ratio and injected over a Superose 6 Increase 3.2/300 column (GE Healthcare) equilibrated in Buffer D (10 mM Tris pH 8.0, 100 mM NaCl, 0.06% FA3, 0.1 mg/mL POPC:POPE:POPG mixed at molar ratio 3:1:1). 3.5 μL of the peak fraction of ProTx2-VSD2-NavAb complex at a concentration of 2 mg/mL was applied to a glow-discharged C-flat holey carbon grid (CF-1.2/1.3-2C, Electron Microscopy Sciences) coated with a thin layer of gold. Grids were blotted in Vitrobot Mark IV (Thermo Fisher) using 5 s blotting time with 100% humidity, and then plunge-frozen in liquid ethane cooled by liquid nitrogen. A total of 25,084 movie stacks were collected with SerialEM (Mastronarde, 2005) on a Titan Krios (Thermo Fisher) operated at 300 kV and equipped with a BioQuantum energy filter operated with a 20eV energy slit with a K2 Summit direct electron detector camera (Gatan). Images were recorded at a nominal magnification of 165,000 x, corresponding to a pixel size of 0.849 \AA per pixel. Each image stack contains 40 frames recorded every 0.25 s giving an accumulated dose of $\sim 41 \text{ e}^-/\text{\AA}^2$ and a total exposure time of 10 s. Images were recorded with a set defocus range of 1.0 to 2.5 μm .

Cryo-EM image processing

The image stacks were processed using cisTEM (Grant et al., 2018). Whole-frame motions were corrected, followed by estimation of contrast transfer function (CTF) parameters and resampling of the output images to 1.2 \AA /pixel. Images with CTF fits to 4.5 \AA or better were selected. 939,063 coordinates were then automatically selected based on an empirical evaluation of maximum particle radius (65 \AA), characteristic particle radius (60 \AA), and threshold peak height (4 SD above noise). Three rounds of 2D classifications into 300 classes were performed to remove false positives and suboptimal particles. The remaining 288,371 particles were used for *ab initio* 3D reconstruction either with C1 or C2 symmetry applied. These particles were then used for iterative 3D classification and auto-refinement without or with a mask. The Fab molecules were flexible and of lesser biological interest, so different masks to focus the 3D classification and refinement on ProTx2-VSD2-NavAb were applied. During 3D refinement, the masked regions of the map were low-pass filtered to 15 \AA . The best two classes representing S4 down (VSD2-deactivated) and S4 up (VSD2-activated) states of VSD2 contained $\sim 53 \text{ k}$ and 187 k particles and were auto-refined with C2 symmetry to $\sim 3.6 \text{ \AA}$ (FSC = 0.143), using data up to $1/8 \text{ \AA}^{-1}$ during refinement. The FSC curve for the S4 down map dropped rapidly around 4.4 \AA before hovering around $\sim 0.15\text{--}0.2$ until $\sim 3.6 \text{ \AA}$, indicating very low SNR at those resolutions, so we estimated its resolution to be $\sim 4.2 \text{ \AA}$. Local resolution of the maps was estimated using a re-implementation of the blocres algorithm (Cardone et al., 2013) within cisTEM, using a box size of 20 pixels. Maps were sharpened by amplitude scaling to yield a flat rotational power spectrum from $1/10 \text{ \AA}^{-1}$ to the estimated resolution, at which radius a cosine-edge low-pass filter was applied. For model-building and figure preparation, maps were filtered locally according to the estimated local resolution.

Cryo-EM model Building

The crystal structure of ProTx2-VSD2-NavAb was used as an initial model and docked to the cryo-EM maps by rigid-body fitting. The model was manually adjusted in Coot and refined using phenix.real_space_refinement (Adams et al., 2010).

Automated whole cell patch clamp recordings

Automated patch clamp (APC) recordings were performed in whole-cell configuration by using either a SyncroPatch 768PE system (Nanion Technologies, Germany) or an 8-channel Patchliner system (Nanion Technologies, Germany) with single-hole medium resistance ($\sim 2\text{--}6 \text{ M}\Omega$) borosilicate glass planar chips. Pulse generation and data collection were performed with PatchController384 V1.5.2 and DataController384 V1.5.0 software from SyncroPatch system. Currents were sampled at 10 kHz and filtered with Bessel filter. Series resistance was compensated 80% with leak artifacts subtraction. Seal resistance (R_{seal}) was calculated using built-in protocols, and high quality recording data was obtained by auto filtering 3 quality control criteria: cell catching ($> 10 \text{ M}\Omega$), seal resistance ($> 500 \text{ M}\Omega$) and baseline current amplitude ($> 500 \text{ pA}$), and follow with manual inspection. Patch-clamp peak current measurements are presented as the means \pm SEM.

For all APC Nav channel recordings, the intracellular solution contained (in mM): 50 CsCl, 60 CsF, 10 NaCl, 20 EGTA and 10 HEPES (pH 7.2, osmolarity 285 mOsm), and extracellular solution contained (in mM): 80 NaCl, 60 NMDG, 4 KCl, 2 CaCl_2 , 1 MgCl_2 , 5 Glucose and 10 HEPES (pH 7.4, osmolarity 300 mOsm). Except in ion strength experiments, extracellular solutions were prepared by changing sodium and glucose concentrations to reach molar ionic strength (M) 0.03 to 0.17, with maintaining 300 mOsm. The holding membrane potential (V_m) for all experiments was set at -120 mV unless otherwise noted. For current–voltage (IV) relationship studies, voltage gated sodium currents were elicited by depolarizing voltage steps from -80 mV to $+40 \text{ mV}$ for 20 ms (5 mV increments). While half steady-state inactivation ($V_{1/2}$) studies were performed by preconditioning V_m from -120 to 0 mV (5 mV

increments) for 500 ms then followed with stimulation pulse at -10 mV for 20 ms. Current activation and inactivation curves of the channels were plotted using the following Boltzmann equation: $G_{Na}/G_{Na,max} = 1/(1 + \exp((V+V_{50})/kV))$, for which the G_{Na} (conductance) value for each clamped oocyte was determined by dividing the peak Na^+ current by the driving force ($V_m - E_{Na}$). In pharmacological tests, current was elicited every 2 s, 5 min before and 25 min after applying compound. For compound effect analysis, compound inhibition was calculated as the percentage of peak current (I) decrease from before compound application ($I_{Baseline}$) to the end of 25 min compound application (I_{End}) and both being normalized to the end of experiment full block current (I_{Full_block}). All IC_{50} values were calculated by using Prism (version 6.05, Graphpad, CA) four-parameter Hill equation fitting of the dose-response curve, with each point $n = 3 \sim 100$. MTS reagents were purchased from Toronto Research Chemicals (Canada).

QUANTIFICATION AND STATISTICAL ANALYSIS

Cryo-EM

Global resolution estimations of cryo-EM density maps are based on the 0.143 Fourier Shell Correlation criterion (Rosenthal and Henderson, 2003).

Electrophysiology

All functional assay toxin potency error bars represent 95% IC_{50} confidence range by using Prism four parameters regression fitting with R2 criterion as 0.95.

DATA AND SOFTWARE AVAILABILITY

The accession number for the ProTx2-VSD2-NavAb channel crystal structure is PDB: 6N4I. The accession numbers for the ProTx2-VSD2-NavAb (VSD2-activated) cryo-EM model and map are PDB: 6N4Q and EMDB: EMD-0341, respectively. The accession numbers for the ProTx2-VSD2-NavAb (VSD2-deactivated) cryo-EM model and map are PDB: 6N4R and EMDB: EMD-0342, respectively. Further information about sample preparation, data collection, or data processing can be directed to the Lead Contact.

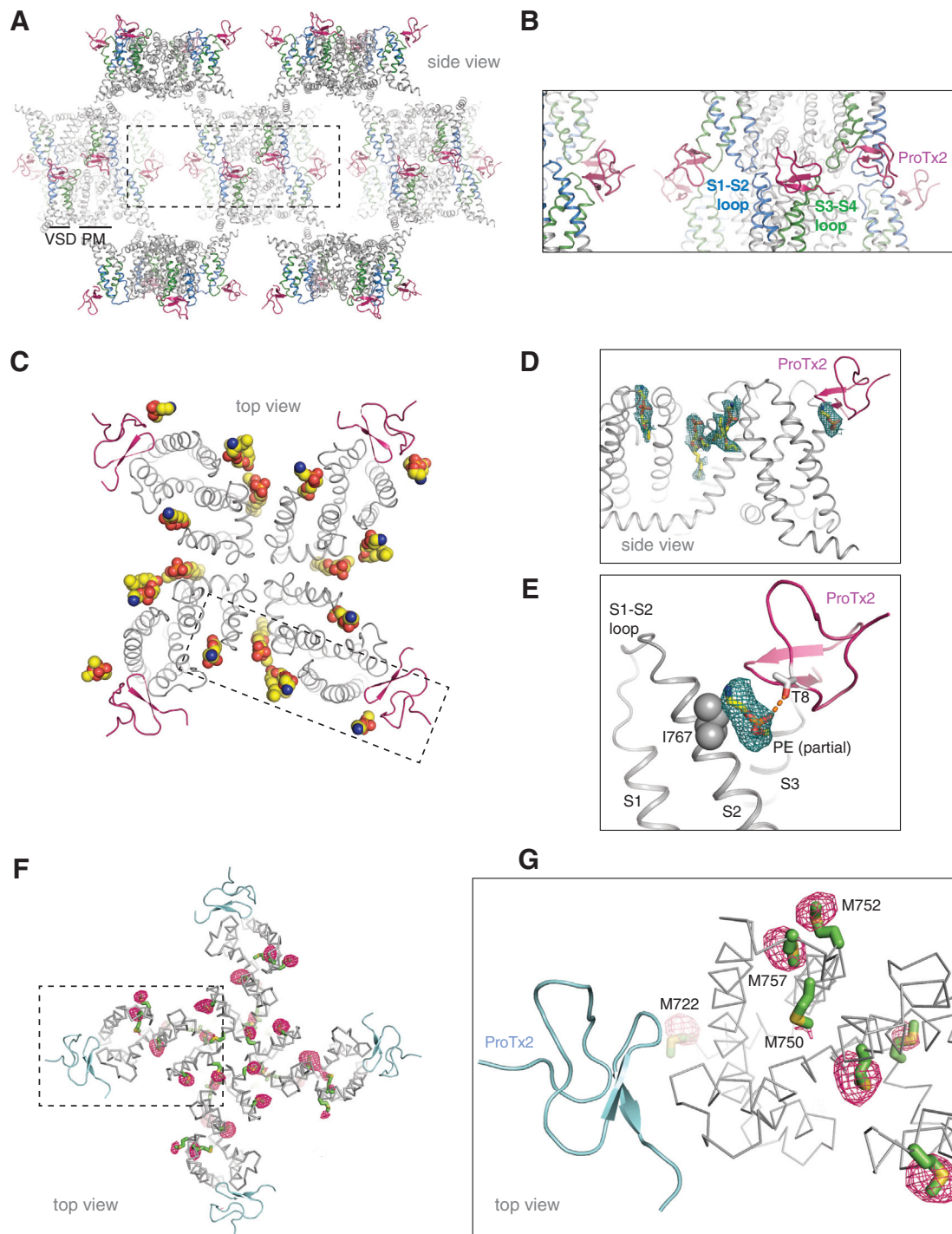


Figure S2. Crystal Packing, Phospholipids, and SeMet Derivative of the ProTx2-VSD2-NavAb Channel, Related to Figure 1

S2A. The ProTx2-VSD2-NavAb channel crystallized in a Type 1 lattice as expected for a protein crystallized from a detergent-lipid mix where a membrane bilayer-like organization can be appreciated. S2B. Close-in view of the crystal lattice packing environment shows that ProTx2 is free from lattice contacts outside of the VSD2 receptor site. The S1-S2 and S3-S4 loops do approach one another from neighboring molecules within the asymmetric unit but no direct contacts between the S3-S4 loops are observed (i.e., the S3-S4 loops approach only within ~ 7 Å of one another). S2C. Top view of the ProTx2-VSD2-NavAb complex with modeled phospholipids assigned as phosphatidylethanolamine shown in yellow sphere representation. S2D. Membrane view with modeled lipids in yellow stick representation with a 2Fo-Fc map calculated *before* any lipids were modeled or refined, rendered at 1 σ , carved at 3 Å. S2E. Close-in view of extra density assigned as PE-lipid in contact with I767 (S2) and within hydrogen bonding distance of ProTx2 T8 (depending on T8 side-chain rotamer). S2F. Top view of the VSD2-NavAb SeMet channel with anomalous difference peaks shown in pink mesh, rendered at 4 σ , and carved at 10 Å. S2G. Same as in panel F, but a close-in view.

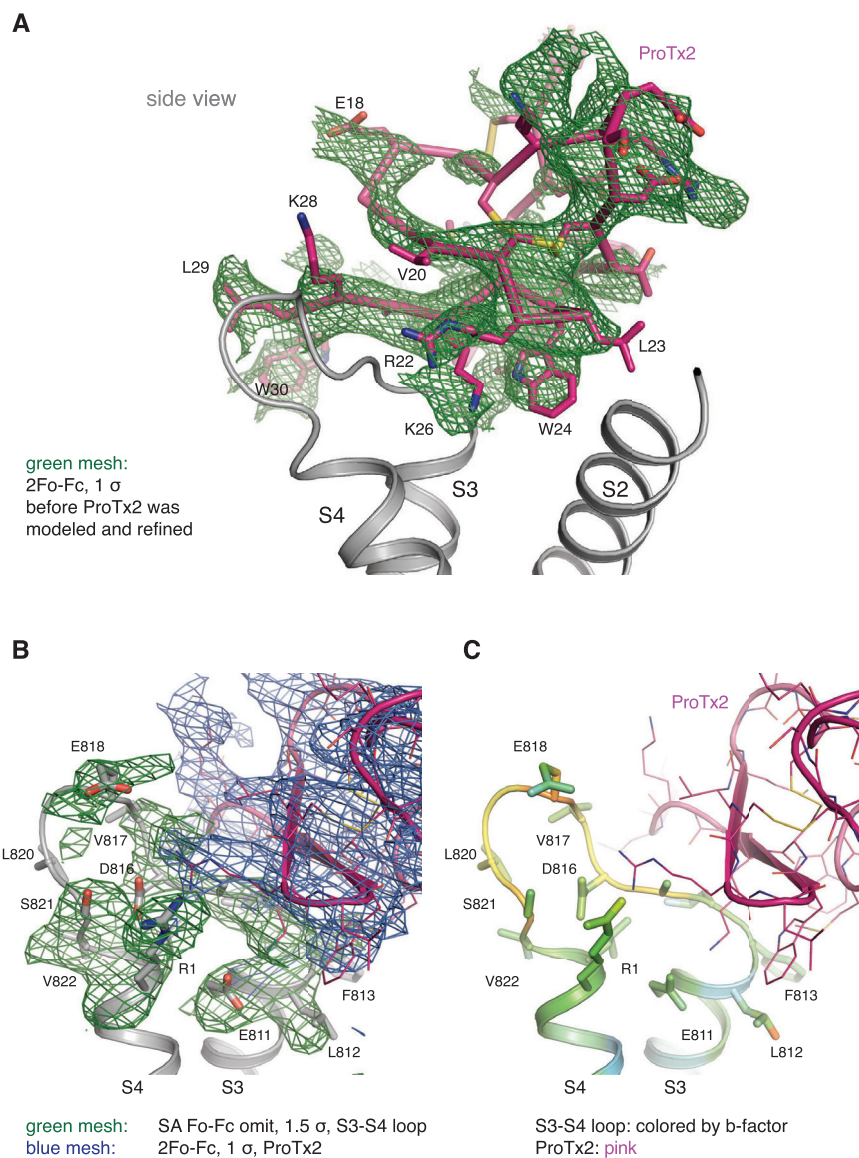


Figure S3. ProTx2 and the VSD2 Receptor Site, Related to Figures 1, 2, and 3

S3A. View from the pore domain, a 2Fo-Fc map (green mesh) calculated *before* any portion of ProTx2 was modeled or refined is rendered at 1 σ , carved at 3 Å. S3B. S3-S4 loop portion of the ProTx2 receptor site is shown (gray sticks) with a simulated annealing (SA) Fo-Fc omit map, where residues E811-R824 from all chains were omitted from the calculation (green mesh), rendered at 1.5 σ , carved at 3 Å. For comparison, a 2Fo-Fc map is rendered only over ProTx2 (blue mesh) at 1 σ , carved at 3 Å. Only VSD2 residues have been labeled for clarity. S3C. Same view as in panel B with maps omitted for clarity, where B-factors for the S3-S4 loop region are shown and colored from low to high (blue to red), respectively. Chain C of VSD2 has been shown here as a representative example, where equally strong electron density features are observable in chain A. Only VSD2 receptor site residues have been labeled for clarity.

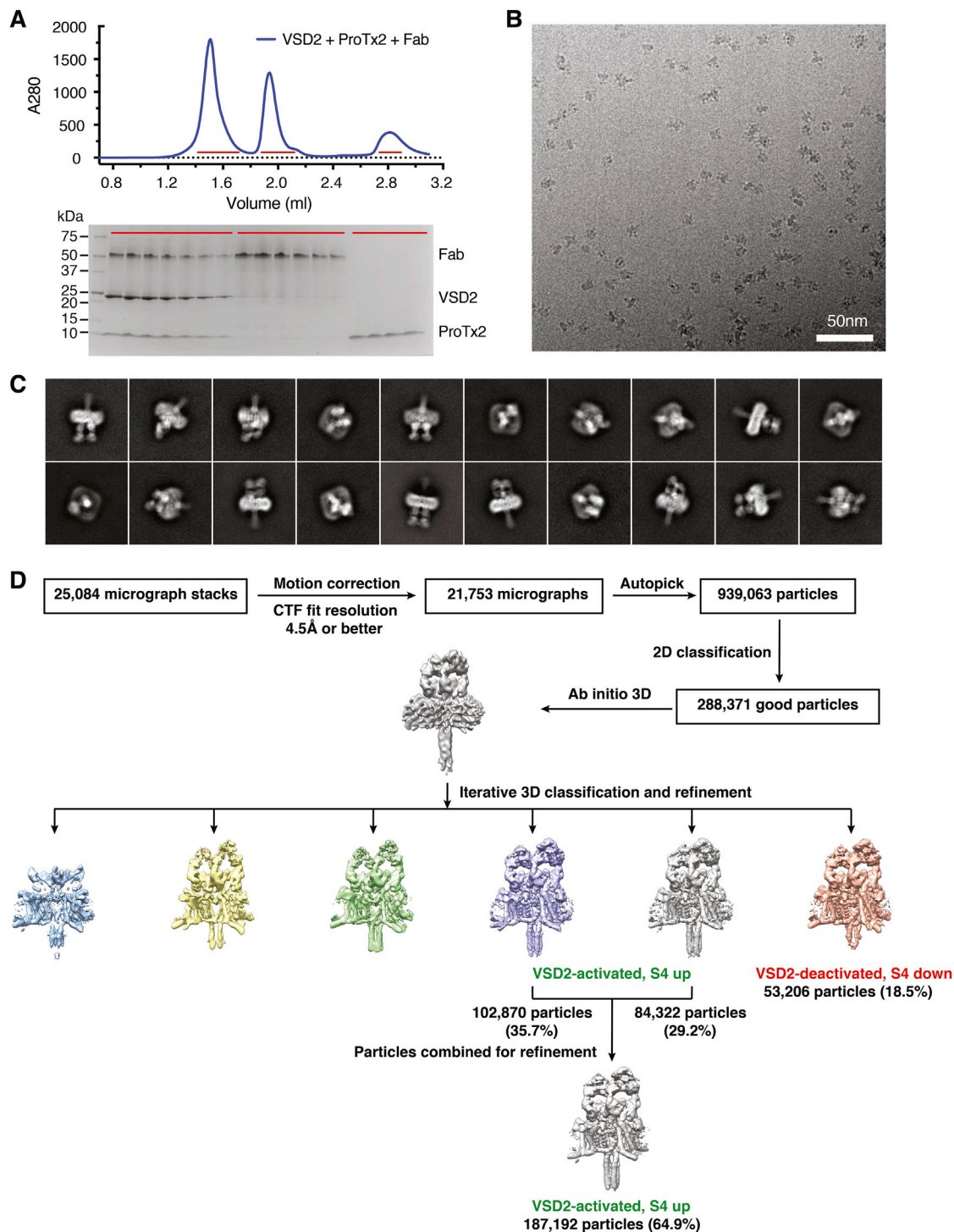


Figure S4. Cryo-EM Sample Preparation and Analysis of the ProTx2-VSD2-NavAb Channel Complex, Related to Figures 5 and 6

S4A. The same channel construct and detergent-lipid conditions were used to prepare ProTx2-VSD2-NavAb channel complexes for cryo-EM analysis as had been used for crystallography. A Fab fragment that targets the PM of the NavAb channel was added to increase the molecular weight of the complex and assist in particle alignment. Size exclusion chromatography profile of the ProTx2-VSD2-NavAb channel-Fab complex is shown. S4B. A representative cryo-electron micrograph of the complex. S4C. Representative 2D class averages. S4D. An overview of the cryo-EM data processing. After various treatments to mask the VSD2 and Fab regions of the channel, 2 major classifications that we refer to as the activated and deactivated conformations of VSD2 emerged.

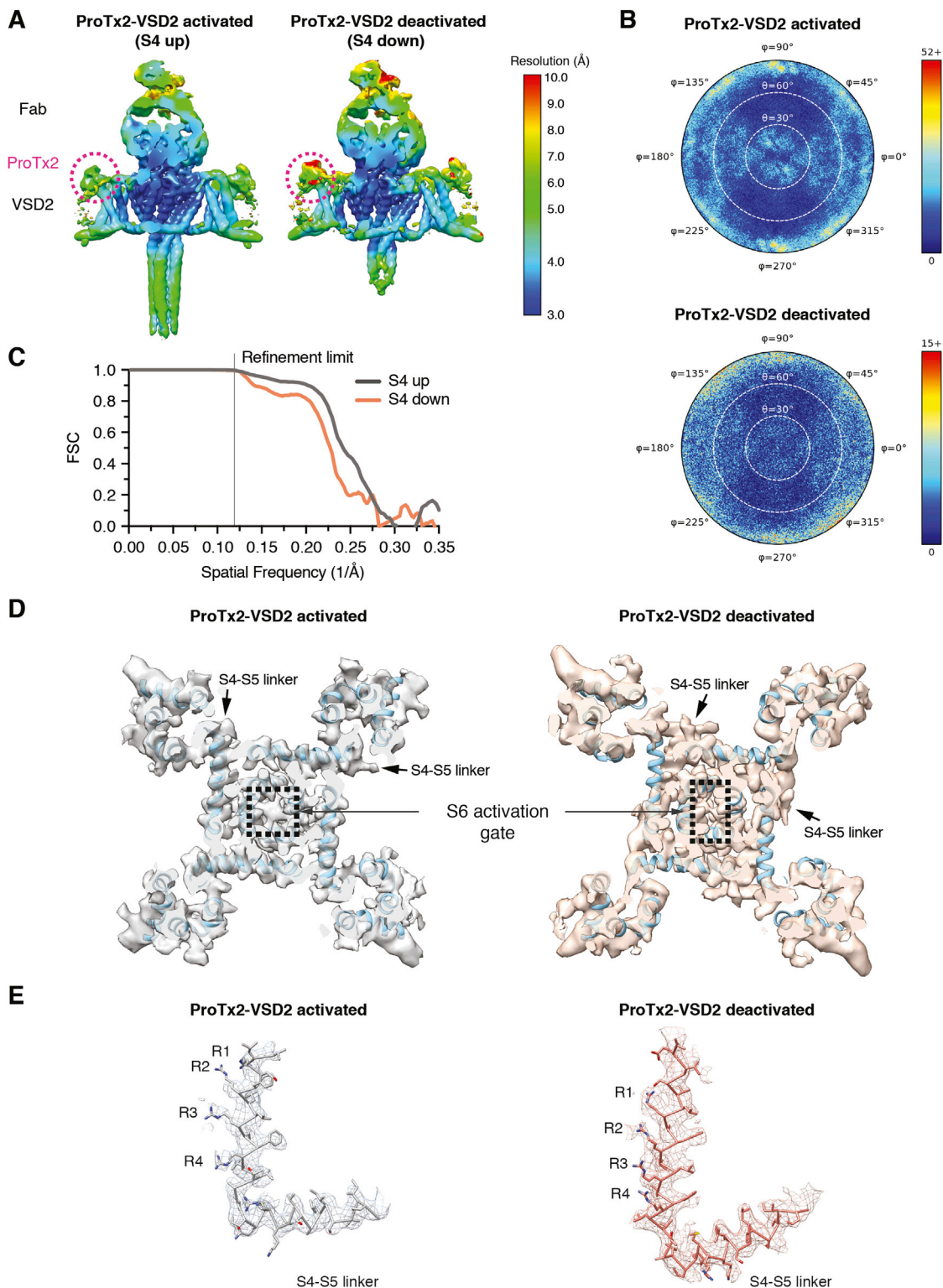


Figure S5. Cryo-EM Analysis of the ProTx2-VSD2-NavAb Channel Complex, Related to Figures 5 and 6

S5A. Local resolution of maps. S5B. Orientation distribution of particles for the final 3D reconstructions. S5C. Fourier shell correlation curve for the cryo-EM maps. Frequencies beyond $1/8 \text{ \AA}^{-1}$ were not used during refinement, as indicated by the vertical line. S5D. A section through S6-activation gate from the VSD2-activated state (gray) shows good correspondence with ProTx2-VSD2-NavAb crystal structure (cyan). Density corresponding to the S6 helices forms a local four-fold symmetric enclosure around the central pore axis. By comparison, a section through activation gate from the VSD2-deactivated state (orange) shows poor

(legend continued on next page)

correspondence with ProTx2-VSD2-NavAb crystal structure over the S4-S5 linkers and S6 activation gate. Arrows indicate the movement and repositioning of the S4-proximal portion of the S4-S5 linker in the deactivated state map relative to the ProTx2-VSD2-NavAb crystal structure (cyan). Rearrangements impinge on the S6 helices, which leads to a constriction of the activation gate where two S6 helices move toward the central pore axis, whereas the other S6 helices are consequently pushed away. S5E. View of the S4 and S4-S5 linker regions in the VSD2-activated (left) and VSD2-deactivated (right) state maps. Mesh isosurfaces of the cryo-EM maps are shown, along with C α backbone traces and side chain representations of the models refined into them. Both PMs were aligned vertically, so that the panels are in vertical register.

A

	S1N	S1	S2	
Nav1.7 VSD1	LRRISIKILVHSLF	SMLIMCTILTNCIFMTMNNP	-----PDWTKNVEYFTFTGIYTFESLVKILARGFCVGEFT	184
Nav1.7 VSD2	FKKCIYFIVMDPFVDLAITICIVLNTL	FMAMEHHPMT--EEFKNVLAIGNLVFTGIFAEMVLKLIAMD	----PYE	791
Nav1.7 VSD3	IRKTCYKIVEHSWFESFIVLMILLSSGALAFEDIYIERKTKIILEYADKIFTYIFILEMLLKIAYG	----	YKT	1254
Nav1.7 VSD4	IQCIFDLVTNQAFDISIMVLICLNMVTMMVKEGQS	--QHMTEVLYWINVVFILFTGECVLKLI	SLR----	H-Y 1572
	::	:: . . . *	* . : . : . :	:
			:	:
			:	:
			:	:
			:	:

	S3	S4	S4-S5 linker	
Nav1.7 VSD1	FLRDPWNWLD	FVVIVFAYLTFE	VNL-----GNVSALRTFRVLRAL	KTISVIPGLKTI
Nav1.7 VSD2	YFQVGWNI	FDSLIVTSLV	ELFLADV-----EGLSVLRSF	RLLRVFKLAKSWPTLNMLIKI
Nav1.7 VSD3	YFTNAWCN	LDLIVDVSLV	TLVANTL	LGYS---DLGPIKSLRTLRLRPLRALS
Nav1.7 VSD4	YFTVGNWNI	FDVVVVIISIV	GMFLADLI	ETYFVSPTLFRVIRLARIGRIILRVK
	::	*	::	::
		::	::	::
		::	::	::
		::	::	::
		::	::	::

B

	S1N	S1	S2	
Nav1.1 VSD2	VKHVNLV	VMDPFVDLAITICIVLNTL	FMAMEHYPMTEHFN	NVLTVG
Nav1.2 VSD2	VKHLVNLV	VMDPFVDLAITICIVLNTL	FMAMEHYPMTEQFSSV	LSVGNLVFTGIFTAEMFLKII
Nav1.3 VSD2	VKHLVNLV	VMDPFVDLAITICIVLNTL	FMAMEHYPMTEQFSSV	LTVG
Nav1.4 VSD2	FKNIIHLI	VMDPFVDL	GITICIVLNTL	FMAMEHYPMTEHFDN
Nav1.5 VSD2	IKQGVKLV	VMDPFDL	ITITMCIVLNTL	FMALAHYNTSEFEEM
Nav1.6 VSD2	LKEIVNLV	VMDPFVDLAITICIVLNTL	FMAMEHHPMPQF	EHVLA
Nav1.7 VSD2	FKKCIYFIVMDPFVDLAITICIVLNTL	FMAMEHHPMTEEFKNV	LAIGNLVFTGIFAEMVLKLI	AMD
Nav1.8 VSD2	LKTI	LFGLVDPFAELTITL	CI	VNTIFMAMEHGMSPTEAM
	. *	:	::	::
	::	::	::	::
	::	::	::	::
	::	::	::	::
	::	::	::	::

	S3	S4	S4-S5 linker	
Nav1.1 VSD2	YFQEGWNI	FDGFI	VTLVSLV	ELGLANVEGLSVLRSF
Nav1.2 VSD2	YFQEGWNI	FDGFI	VSLVSLMELGLANVEGLSVLRSF	RLLRVFKLAKSWPTLNMLIKI
Nav1.3 VSD2	YFQEGWNI	FDGI	IVSLSMELGLSNVEGLSVLRSF	RLLRVFKLAKSWPTLNMLIKI
Nav1.4 VSD2	YFQEGWNI	FDSI	IVTLVSLV	ELGLANVQGLSVLRSF
Nav1.5 VSD2	YFQEGWNI	FDSI	IVTLVSLV	ELGLANVQGLSVLRSF
Nav1.6 VSD2	YFQEGWNI	FDGFI	VSLVSLMELSLADVEGLSVLRSF	RLLRVFKLAKSWPTLNMLIKI
Nav1.7 VSD2	YFQEGWNI	FDSLIVTSLV	ELFLADVEGLSVLRSF	RLLRVFKLAKSWPTLNMLIKI
Nav1.8 VSD2	YFQKKNIF	DCI	IVTVSLL	ELGVAKKGSLSVLRSF
	**	*	*	*
	::	::	::	::
	::	::	::	::
	::	::	::	::
	::	::	::	::

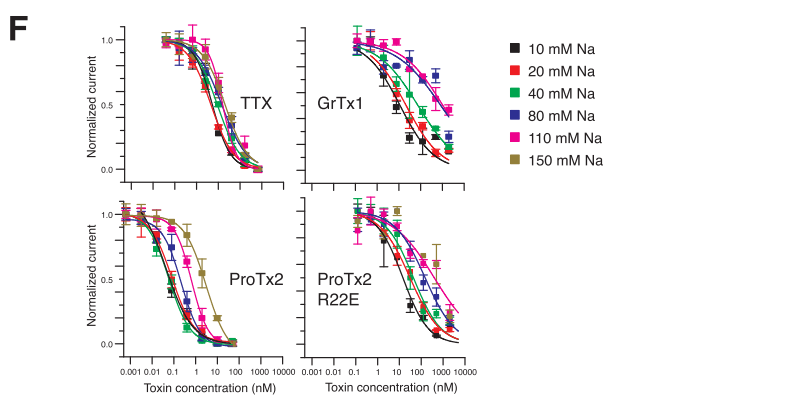
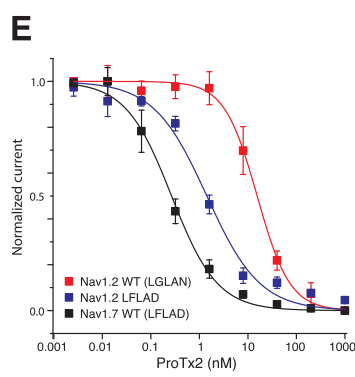
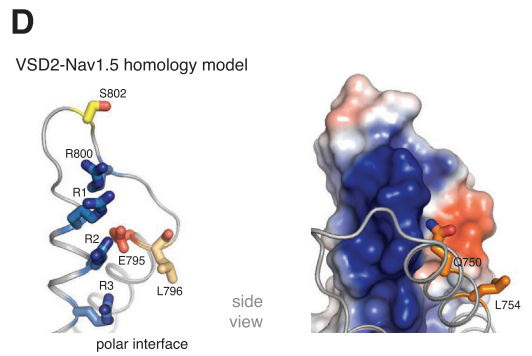
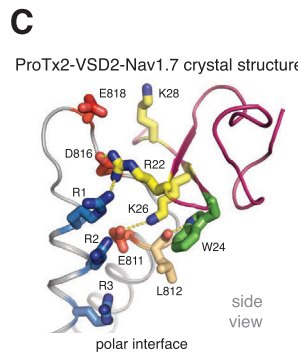


Figure S6. VSD2 Sequence Alignments, Homology Models, and Ionic Strength Effects, Related to Figures 1, 2, 3, and 4

S6A. Sequence alignment of VSD1-VSD4 from human Nav1.7 with the FLAD motif (conserved in VSD2 and VSD4) highlighted in purple. S1-S2 and S3-S4 residues grafted on the VSD2 construct are highlighted in blue and green, respectively. S6B. Sequence alignment of VSD2 from all human Nav channel subtypes (except for Nav1.9, which diverges considerably in the ProTx2 receptor site region). Residues on the S2 that contact ProTx2 in the Nav1.7 VSD2 complex are highlighted in orange. Acidic residues in the S3-S4 region, some of which contact ProTx2 in the Nav1.7 VSD2 complex, are highlighted in red. The LFLAD motif (or equivalent sequence) is highlighted in purple. S6C-D. Crystal structure and electrostatic surface of the ProTx2-VSD2 Nav1.7 complex is compared to an *in silico* homology model generated for human Nav1.5 over the same region. S6E. Potency of ProTx2 measured on wild-type Nav1.7, wild-type Nav1.2, and a Nav1.2 chimera channel that was substituted in VSD2 from the LGLAN sequence to the LFLAD sequence. Error bars represent mean \pm SEM. S6F. Potencies of the indicated toxins were determined on human Nav1.7 at the ion strengths indicated. Error bars represent mean \pm SEM.